Topology Optimization for the Full-Cell Design of Porous Electrodes in Electrochemical Energy Storage Devices

Hanyu Li[1], Giovanna Bucci[1], Nicholas W. Brady[1], Nicholas R. Cross[1], Victoria M. Ehlinger[1], Tiras Y. Lin[1], Miguel Salazar de Troya[1], Daniel Tortorelli[1], Marcus A. Worsley[1] and Thomas Roy[1*]

[1]Lawrence Livermore National Laboratory - 7000 East Ave, Livermore, CA 94550, USA.

*Corresponding author(s). E-mail(s): roy27@llnl.gov;

Abstract

In this paper, we introduce a density-based topology optimization framework to design porous electrodes for maximum energy storage. We simulate the full cell with a model that incorporates electronic potential, ionic potential, and electrolyte concentration. The system consists of three materials, namely pure liquid electrolyte and the porous solids of the anode and cathode, for which we determine the optimal placement. We use separate electronic potentials to model each electrode, which allow interdigitated designs. As the result, a penalization is required to ensure that the anode and cathode do not touch, i.e. causing a short circuit. We compare multiple 2D designs generated for different fixed conditions, e.g. material properties. A 3D design with complex channel and interlocking structure is also created. All optimized designs are far superior to the traditional monolithic electrode design with respect to energy storage metrics. We observe up to 750% increase in energy storage for cases with slow effective ionic diffusion within the porous electrode.

Keywords: Topology optimization, Electrochemistry, batteries, supercapacitors

1 Introduction

Electrochemical energy storage devices provide a shift away from fossil fuels by enabling electric vehicles and supporting the adoption of intermittent renewable energy sources (Chu and Majumdar, 2012; Chu et al, 2016; Gür, 2018). Batteries and capacitors are examples of such devices that are ubiquitous in modern technologies. And thus improving their performance is crucial for the green energy transition.

The electrochemical charge storage mechanisms can be broadly grouped into two types: charge separation and Faradaic charge-transfer reactions (Simon et al, 2014). In the former, electrostatic double-layer capacitors (EDLCs) store energy by forming an electric double layer at the interface between the electrodes and electrolyte. This is different from the latter

wherein electrons are transferred via reduction and oxidation (i.e. *redox*) reactions. Such reactions are the principal energy storage mechanism of batteries, which utilize slow kinetics and therefore lower power density but enable much higher energy density than EDLCs. As a middle ground, pseudocapacitors use fast redox kinetics, resulting in smaller energy density than batteries but larger than EDLCs while also demonstrating high power density (Simon et al, 2014).

Batteries and capacitors share a common design: two porous electrodes, namely the anode and the cathode, are immersed in a liquid electrolyte and separated by a membrane or simply an electrolyte-filled gap. The traditional monolithic porous electrode cell illustrated in Fig. 1 consists of two slabs described by a uniform porosity and surface area to volume ratio. The electrodes are typically assemblies of micron-scale

conductive particles. Electrochemical reactions occur over the interface between the electrode-particles and the electrolyte. As such, cell-design criteria primarily focus on maximizing the surface area to volume ratio while minimizing resistances related to electron or ion transport (Wang et al, 2008), as these criteria enable higher currents, power outputs, and energy storage.
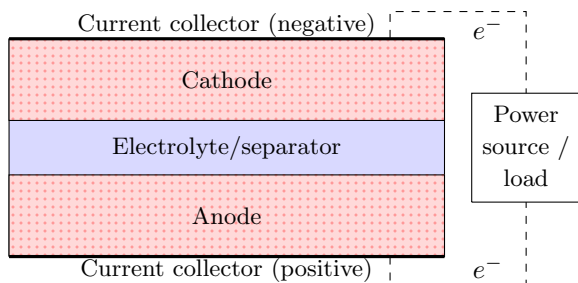

Fig. 1: Diagram of a traditional monolithic electrochemical energy storage device.

Simply maximizing electrochemical surface area, in the attempt to increase energy density, often deteriorates ionic transport within the electrode by replacing the pore network for ion transport with an extremely tortuous path (Wang et al, 2008). Such paths restrict ionic penetration into the monolithic electrodes and thus reduce their effectiveness. Fortunately, promising alternatives to these monolithic designs are emerging; e.g. electrode designs with geometric features, multiple lengthscales and/or materials, and spatially varying porosity (Beck et al, 2021a; Trembacki et al, 2019; Zekoll et al, 2018; Gao et al, 2023; Yang et al, 2022). These new designs are made possible thanks to new advanced manufacturing processes (Chu et al, 2021; Soares et al, 2021; Chandrasekaran et al, 2023). It is this nearly complete control over the electrode design that raises the question of what these designs should be.

One approach to increase the energy density consists in increasing the thickness of conventional slab electrodes and reducing the number of cells needed in a stack. This approach allows to reduce the weight associated with non-active materials such as current collectors, foils and separators (Heubner et al, 2021). However, the electrode areal capacity is limited by the ion transport within the tortuous electrode structure, and typical commercial-electrodes have a thickness in the range of 100-150 µm. (Heubner et al, 2021; Xu et al, 2019; Kuang et al, 2019). Further increasing the electrode thickness (and the areal capacity) leads to a point of diminishing returns in volumetric energy

density for charge/discharge rates relevant to electric-vehicle applications (Singh et al, 2015; Zheng et al, 2012; Gallagher et al, 2015).

Thicker electrodes with three-dimensional features, in contrast to conventional slabs, have been previously fabricated and tested (Long et al, 2004, 2020), demonstrating the importance of providing structure and low-tortuosity transport pathways that facilitate ion transport in the electrolyte. A categorization of the various three-dimensional designs has been proposed by Hung et al (2022): the electrodes may be individually shaped and separated by a planar separator, which is either solid or porous, or completely intertwined with one another. In particular, an interdigitated design, where alternating planar fins or rods protruding from the cathode and anode separated by the electrolyte, has demonstrated increased power and energy performance (Hung et al, 2021; Zadin et al, 2011). Similar three-dimensional interpenetrating structures have been investigated for microbatteries and wearable devices applications (Lyu et al, 2021; Zeng et al, 2014; Wang et al, 2017). The non-planar structures improve performance via increased surface area to volume ratios to promote reaction and increased ionic diffusion through complex pathways to promote mass transport (Trembacki et al, 2019; Chen et al, 2020), therefore enabling high power and fast charging lithium-ion batteries (Chen et al, 2020; Zekoll et al, 2018). However, because the current distribution and concentration profiles in these interdigitated and interpenetrating electrodes are highly non-uniform (Hart et al, 2003; Trembacki et al, 2019), their performance becomes strongly dependent on the electrode and electrolyte properties, e.g. specific surface area and conductivity, thus motivating the need for a systematic design optimization paradigm.

Computational techniques such as topology optimization offer a promising opportunity to design optimal porous electrodes. Density-based topology optimization was initially formulated as a mass distribution problem in which the volume fraction field is optimized to maximize the stiffness of a linear elastic structure subject to a mass constraint Bendsøe (1989). Topology optimization has since been adapted to design electrochemical devices. Yaji et al (2018); Chen et al (2019); Lin et al (2022) design the channels that transport the electrolyte fluid to the porous electrodes in redox flow batteries. Behrou et al (2019); Wang et al (2023); Qu et al (2023) similarly design channels in fuel cells to minimize electrical and pumping power losses while maximizing power density. Heterogeneous porosity fields have been designed for lithium-ion batteries (Ramadesigan et al, 2010; Golmon et al, 2012; Xue et al, 2015), and redox flow batteries (Beck et al, 2021b).

Topology optimization has been used in Roy et al (2022) to design redox porous electrodes and EDLC electrodes. This study, which only considers a half cell, i.e. a single electrode, generates designs for a wide range of fixed dimensionless groups encapsulating material parameters, electrode length scale, and operating conditions. The best performance improvement over monolithic designs was achieved when ionic transport within the porous material is slow. Batista et al (2023) used a similar optimization framework to design a supercapacitor electrode, which was then fabricated using additive manufacturing. The optimized electrode exhibited nearly twice the volumetric capacitance over a lattice structured electrode. The models used to predict the response in these previous studies assumed no concentration gradients; the model in a more recent optimization study by Alizadeh et al (2023) included mass accumulation and entropy effects. In this work, we optimize both electrodes simultaneously using a full-cell model that includes mass transport.

A fundamental flaw with density-based topology optimization is the use of the material volume fraction field as the control. As such, regions in the optimized designs contain mixtures of materials, which is not possible, i.e. we must have so-called $0-1$ designs in which a distinct material resides at each location. The size of these mixed "intermediate" material regions is minimized by using clever penalization schemes in the topology optimization problem formulation. For structural optimization, the penalization is relatively straightforward because of the explicit trade-off between the structural stiffness and mass cf. e.g. the Simple Isotropic Material with Penalization (SIMP) (Bendsøe, 1989). For electrochemical energy storage systems, the trade-off between ion/electron transport and chemical activity is less obvious, thus special care is required when devising penalization schemes. Schemes that concurrently increase ohmic loss and reduce energy storage in intermediate material regions have proven effective (Roy et al, 2022; Batista et al, 2023). Developing effective penalization schemes for topology optimization can be very tedious. However those that conquer this battle are rewarded with a very effective design tool.

In this manuscript, we use topology optimization to design full-cell electrochemical energy storage devices. In Sect. 2, we review topology optimization concepts, and describe the boundary propagation method required for the two-electrode optimization. Next, in Sect. 3, we introduce the simulation model, i.e. the Nernst-Planck equation for a binary electrolyte with redox reactions and electrostatic double layer capacitance. Implementation and solver details are provided in Sect. 4. Following that, in Sect. 5,

the optimization problem is formulated and solved to generate designs for various key dimensionless groups encapsulating device length scale and material parameters such as conductivity and reaction rate. We also compare the performances of two optimized designs against traditional monolithic electrodes to demonstrate effectiveness of the optimization. Next, we showcase a 3D design, possessing complex channels and interlocking features. We conclude in Sect. 6 with some final discussion.
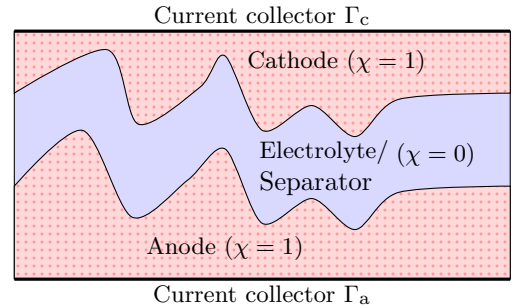
2 Topology optimization

Fig. 2: Two-dimensional design space of a full cell with porous electrodes.

Our topology optimization problem concerns the material indicator field χ in cell domain Ω defined such that $\chi(\mathbf{x}) = 1$ indicates that the solid porous electrode material occupies $\mathbf{x}$, whereas $\chi(\mathbf{x}) = 0$ indicates that the separator or pure liquid electrolyte occupies $\mathbf{x}$, cf. Fig. 2. Over this domain we solve the model equations $F(\chi, \Phi_1, \Phi_2, c) = 0$ to be introduced in Sect. 3, for the electronic potential Φ_1, ionic potential Φ_2, and salt concentration c. These pieces are used to define the porous electrodes topology optimization problem, i.e.

$$\min_{\chi\colon \Omega \to \{0,1\}} \theta_0(\chi) = \int_\Omega \pi(\chi, \Phi_1, \Phi_2, c)\, dV,$$

$$\text{s.t. } \theta_i(\chi) = \int_\Omega g_i(\chi, \Phi_1, \Phi_2, c)\, dV \le 0,\ i = 1, \ldots, m,$$

$$\text{and } F(\chi, \Phi_1, \Phi_2, c) = 0.$$

$$(1)$$

Here, θ_0 is the cost function to be minimized and θ_i are the m design constraint functions, with local functions π and g_i to be defined in Sect. 5.1.

Since the electrode phase is comprised of separate anode and cathode materials, a three-phase (three-material) optimization formulation would be natural (Sigmund and Torquato, 1997; Watts and Tortorelli, 2016). This three-phase approach requires a

second material indicator field that would delineate the anode and cathode phases. However, since cathode and anode are in contact with different boundaries Γ_c and Γ_a (see Fig. 2), we instead use a boundary propagation method (Sá et al, 2022) for this delineation, cf. Sect. 2.2. Thus, we optimize with respect to a single field χ.

In the context of density-based topology optimization (Bendsøe, 1989), the discrete nature of the design field χ prevents the application of gradient-based optimization algorithms. Because of this, and at the risk of not obtaining $0-1$ designs, we replace $\chi\colon \Omega \to \{0,1\}$ with a continuous volume fraction variable $\rho\colon \Omega \to [0,1]$. Additionally, special care is required to ensure that optimization problem is well-posed. These concerns are remedied using filtering detailed in Sect. 2.1 and material penalization described in Sect. 5.1.

2.1 Filtering

Topology optimization problems are often ill-posed. Their "solutions" are characterized by non-converging sequences of structures with highly oscillatory material distributions. One option to obtain a well-posed problem imposes a feature length scale on the design by filtering ρ to obtain the smoothed field $\tilde{\rho}$, which is used to define the structures of material distribution (Bruns and Tortorelli, 2001; Bourdin, 2001). In our problem, we use the diffusion-reaction PDE filter described in Lazarov and Sigmund (2011) wherein $\tilde{\rho}$ solves

$$\begin{aligned} -r^2 \nabla^2 \tilde{\rho} + \tilde{\rho} = \rho & \qquad \text{in } \Omega, \\ r^2 \nabla \tilde{\rho} \cdot \mathbf{n} = 0 & \qquad \text{on } \partial\Omega, \end{aligned} \tag{2}$$

for the given design ρ. Fine scale oscillations in ρ are mollified in $\tilde{\rho}$; more mollification occurs as the filter radius r increases.

Unfortunately, the filtered design $\tilde{\rho}$ contains large transitional regions where $\tilde{\rho} \neq \{0,1\}$ and our original design problem only allows for $\chi(\mathbf{x}) \in \{0,1\}$ regions, i.e. $0-1$ designs. To remedy this, the filtered distribution $\tilde{\rho}$ is thresholded to define the field $\bar{\rho}$ such that $\bar{\rho}(\mathbf{x}) = \{0,1\}$ throughout Ω. We can do this by equating $\bar{\rho} = H(\tilde{\rho} - 0.5)$ where H is the unit Heaviside function. However, the lack of differentiability of H is not conducive to our gradient-based optimization. As such, we replace H with a smoothed approximation so that

$$\bar{\rho} = H_{b,k}(\tilde{\rho}) = \frac{\tanh(bk) + \tanh(b(\tilde{\rho} - k))}{\tanh(bk) + \tanh(b(1 - k))}. \tag{3}$$

Here, b controls the sharpness of the $0-1$ transition and k controls the cutoff such that

$$\lim_{b \to \infty} H_{b,k}(\tilde{\rho}) = H(\tilde{\rho} - k)$$

(Guest et al, 2004; Sigmund, 2007; Sigmund and Maute, 2013; Xu et al, 2010). In this way, we obtain

"nearly" $0-1$ designs such that $\bar{\rho}(\mathbf{x}) \approx \{0,1\}$ throughout Ω. Here, we use $b = 4$ and $k = 0.5$ for a mild transition. Although mild, it combines well with the continuous boundary propagation method to identify the extent of the cathode and anode regions. Aggressive thresholding, i.e. larger b values, leads to premature convergence to poor local optima. Because of this, continuation techniques on b are often employed to improve optimization convergence and obtain nearly $0-1$ designs. In this work, we do not use continuation approaches, since the combination of mild thresholding and the interpolation described in 5.1 lead to nearly $0-1$ designs.
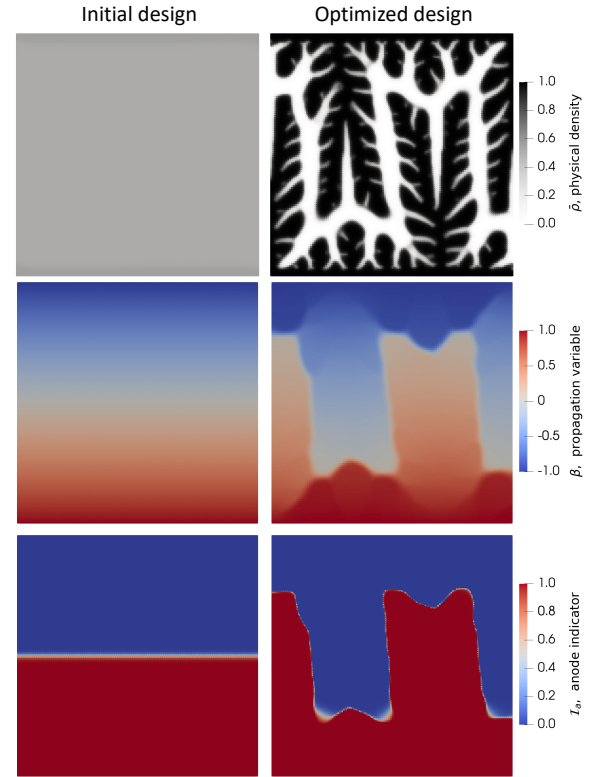
2.2 Continuous boundary propagation

Fig. 3: Physical density $\bar{\rho}$ (top) with its corresponding β (middle) and anode indicator $\mathcal{I}_a$ (bottom) for the initial design (left) and optimized design (right).

We can use $\bar{\rho}(\mathbf{x}) = \{0,1\}$ to determine if electrolyte or electrode resides at $\mathbf{x}$, but we do not know if the electrode is the anode or cathode. This is important

because the anode and cathode may be manufactured with different materials and because we need to separate the anode and cathode regions to avoid a short circuit. Both of these concerns are resolved by using the continuous boundary propagation approach (Sá et al, 2022).

The boundary propagation approach consists of solving the following diffusion-reaction problem cf. Fig. 3 for β:

$$
\begin{aligned}
\bar{\rho}\nabla \cdot \nabla\beta - (1-\bar{\rho})\beta = 0 & \quad \text{in } \Omega, \\
\beta = 1 & \quad \text{on } \Gamma_{\mathrm{a}}, \\
\beta = -1 & \quad \text{on } \Gamma_{\mathrm{c}}, \\
\nabla\beta \cdot \mathbf{n} = 0 & \quad \text{on } \partial\Omega/\Gamma_{\mathrm{c}} \cup \Gamma_{\mathrm{a}}.
\end{aligned}
\tag{4}
$$

In electrode regions ($\bar{\rho} = 1$), the equation reduces to $\nabla \cdot \nabla\beta = 0$, and in electrolyte regions ($\bar{\rho} = 0$), it reduces to $\beta = 0$. By prescribing $\beta = 1$ and $\beta = -1$ on anode and cathode current collector boundaries, namely Γ_a and Γ_c, we are assured that $0 \leq \beta \leq 1$ in the anode and $-1 \leq \beta \leq 0$ in the cathode. The resulting β is transformed into differentiable indicator functions for the anode and cathode regions such that

$$
\begin{aligned}
\mathcal{I}_{\mathrm{a}}(\beta) &= H_{b,k}\left(\frac{\beta+1}{2}\right), \\
\mathcal{I}_{\mathrm{c}}(\beta) &= H_{b,k}\left(\frac{-\beta+1}{2}\right),
\end{aligned}
\tag{5}
$$

with $k = 0.5$.

Examples of $\bar{\rho}$ distributions, their corresponding β propagation, and anode indicator computed with $b = 100$ are illustrated in Fig. 3. To summarize, $\bar{\rho}$ distinguishes between solid electrode and liquid electrolyte regions, and β produces the indicator fields $\mathcal{I}_{\mathrm{a}}$ and $\mathcal{I}_{\mathrm{c}}$ to distinguish between anode and cathode regions. The indicator fields are also used to ensure model consistency as discussed in Sect. 3.3.

3 Governing equations

In this section, we introduce the governing equations to model electrochemical energy storage devices with both redox and capacitive charging effects (Johnson and Newman, 1971; Doyle et al, 1993; Newman and Tobias, 1962; Newman and Tiedemann, 1975). Extending the two-potential system described in our previous study (Roy et al, 2022), we solve the Nernst–Planck equation for the ion concentration fields, which affect the charge-transfer and adsorption kinetics, and the electrolyte conductivity. Therefore, accounting for its mass transport improves the predictability of our designs. Battery models may also include ionic diffusion in the solid particles (Doyle et al, 1993; Brosa Planella et al, 2022), however, for simplicity we ignore solid diffusion, which is a reasonable assumption when the electrode particles are of the order of

$1\ \mu m$ in size. Additionally, we assume that the anode and cathode have identical material properties.

3.1 Physical model

We consider a binary electrolyte in which the cation participates in the redox reaction that produces current density i_n. In the battery, this reaction has the form

$$
s_+ A^{z+} + ne^- \rightleftharpoons s_+ A,
\tag{6}
$$
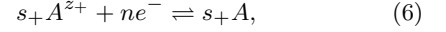
where n is the number of electrons transferred, z_+ is the cation charge number, and $s_+ = n/z_+$ is the cation stoichiometric number. Both cations and anions are adsorbed by double-layer charging, which produces current density i_c. The Nernst–Planck equation for the positive (c_+) and negative (c_-) charged species concentrations are as follows:

$$
\begin{aligned}
\frac{\partial (\epsilon c_+)}{\partial t} &= -\nabla \cdot \mathbf{N}_+ + \frac{dq_+}{dq}\frac{1}{z_+ F}ai_c + \frac{s_+}{nF}ai_n \quad \text{in } \Omega, \\
\frac{\partial (\epsilon c_-)}{\partial t} &= -\nabla \cdot \mathbf{N}_- + \frac{dq_-}{dq}\frac{1}{z_- F}ai_c \quad \text{in } \Omega,
\end{aligned}
\tag{7}
$$

where $\mathbf{N}_i$ is the ionic flux for species $i = \pm$, ϵ is porosity, F is the Faraday constant ($96\,485\,\mathrm{C\,mol^{-1}}$), and a is the specific surface area, which equates zero in the liquid electrolyte region. The variation in the amount of adsorbed cations/anions is captured by $\frac{dq_i}{dq}$, where q_i is the adsorbed cation/anion surface charge density in the double layer, and q is the total surface charge density in the double layer. Assuming the absence of cosorption of anions and cations, $\frac{dq_+}{dq} = 1$ and $\frac{dq_-}{dq} = 0$ for a cation responsive electrode, and $\frac{dq_+}{dq} = 0$ and $\frac{dq_-}{dq} = 1$ for an anion responsive electrode (Johnson and Newman, 1971).

We now define constitutive equations for i_n, i_c, and $\mathbf{N}_i$. The redox and capacitive current densities are defined as

$$
\begin{aligned}
i_n &= i_0\left[\exp\left(\frac{\alpha_a F}{RT}\eta\right) - \exp\left(\frac{-\alpha_c F}{RT}\eta\right)\right], \\
i_c &= C_d\frac{\partial (\Phi_1 - \Phi_2)}{\partial t},
\end{aligned}
\tag{8}
$$

where α_a and α_c are the anodic and cathodic charge transfer coefficients, respectively. For simplicity, we assume $\alpha = \alpha_a = \alpha_c$. Here, the exchange current density is $i_0 = Fk_{\mathrm{rxn}}c^\alpha$, where k_{rxn} is the reaction rate and c is the salt concentration defined below. The overpotential $\eta = \Phi_1 - \Phi_2 - U_0$ is obtained from the electronic potential Φ_1, the ionic potential Φ_2, and the equilibrium potential U_0. R ($8.3145\,\mathrm{J\,K^{-1}\,mol^{-1}}$) is the ideal gas constant, T is the temperature, and C_d is the specific capacitance. Note that battery models typically treat U_0 as a function of solid surface concentration (Doyle et al, 1993); for simplicity, we assume

U_0 to be constant. Therefore, the Nernstian loss, which is defined by the change in the equilibrium potential as a function of the concentration, is not modeled. To account for the effect of concentration on ion adsorption, we define $C_d = C_0 \left(\frac{c}{c_0}\right)^{\alpha}$. This nonstandard addition to the model prevents nonphysical extreme capacitive current density in the designs where high reaction rates could lead to ion depletion.

The ionic flux for an individual species is calculated by

$$\mathbf{N}_i = -z_i u_i F c_i \nabla \Phi_2 - D_i \nabla c_i. \tag{9}$$

In the above, u_i is the effective ion mobility and D_i is the effective molecular diffusion coefficient of the species, which satisfy the Nernst-Einstein relationship as

$$D_i = RTu_i. \tag{10}$$

The stoichiometric coefficient and ion charge number are related by

$$z_i = \frac{n}{s_i}. \tag{11}$$

Both relations are useful for nondimensionalization of the governing system. Assuming electroneutrality, we have the constraint

$$\sum_i z_i c_i = 0, \tag{12}$$

which is also equivalent to

$$\sum_i z_i \nu_i = 0, \tag{13}$$

where ν_i is the number of moles of cations or anions per mole of electrolyte. For a binary electrolyte, we can then define the salt concentration as

$$c = \frac{c_+}{\nu_+} = \frac{c_-}{\nu_-}. \tag{14}$$

Considering electroneutrality, equations (7) are combined into one conservation equation for the salt concentration (see Newman and Thomas-Alyea (2012) for the derivation of the salt concentration equation). Combining that with the charge conservation in the electronic and ionic potentials, we obtain the governing field equations that solve for Φ_1, Φ_2, and c (Newman and Tiedemann, 1975):

$$-\nabla \cdot (\sigma \nabla \Phi_1) = -a\,(i_n + i_c) \qquad \text{in } \Omega, \tag{15a}$$

$$-\nabla \cdot (\kappa \nabla \Phi_2) - z_+ \nu_+ F \nabla \cdot ((D_+ - D_-)\nabla c)$$
$$= a\,(i_n + i_c) \qquad \text{in } \Omega, \tag{15b}$$

$$\frac{\partial(\epsilon c)}{\partial t} - \nabla \cdot (D \nabla c) = \frac{s_+}{F n \nu_+} t_- a i_n$$
$$+ \frac{1}{F z_+ \nu_+} \left(t_- \frac{dq_+}{dq} - t_+ \frac{dq_-}{dq} \right) a i_c \qquad \text{in } \Omega, \tag{15c}$$

subject to the boundary and initial conditions:

$$\Phi_1 = 0 \qquad \text{on } \Gamma_{\text{a}}, \tag{15d}$$

$$\Phi_1 = \zeta t \qquad \text{on } \Gamma_{\text{c}}, \tag{15e}$$

$$\nabla \Phi_1 \cdot \mathbf{n} = 0 \qquad \text{on } \partial\Omega \setminus (\Gamma_{\text{a}} \cup \Gamma_{\text{c}}), \tag{15f}$$

$$\nabla \Phi_2 \cdot \mathbf{n} = 0 \qquad \text{on } \partial\Omega, \tag{15g}$$

$$\nabla c \cdot \mathbf{n} = 0 \qquad \text{on } \partial\Omega, \tag{15h}$$

$$\Phi_1(\mathbf{x}, t = 0) = 0 \qquad \text{in } \Omega, \tag{15i}$$

$$\Phi_2(\mathbf{x}, t = 0) = 0 \qquad \text{in } \Omega, \tag{15j}$$

$$c(\mathbf{x}, t = 0) = c_0 \qquad \text{in } \Omega, \tag{15k}$$

for $t \in (0, T]$, where σ is the effective electronic conductivity, κ is the effective ionic conductivity, and c_0 is the initial concentration. The dimensionless quantity t_+ denotes the transference number of the cation; the transference number of the anion is related by $t_- = 1 - t_+$. The boundary conditions describe a linearly increasing potential in time on the cathode current collector, with scan rate ζ.

In the electrode region, the effective transport properties, namely effective electronic conductivity σ, effective ionic conductivity κ, and the effective salt diffusion coefficient or ambipolar diffusivity D are influenced by the tortuosity of the pores. The Bruggeman correlation (Bruggeman, 1935) quantifies tortuosity as a power law of porosity with exponent $\frac{3}{2}$ for packed spheres, and thus the effective transport properties are calculated as

$$\sigma = (1 - \epsilon)^{\frac{3}{2}} \sigma_0, \quad \kappa = \epsilon^{\frac{3}{2}} \kappa_0, \quad D = \epsilon^{\frac{3}{2}} D_0, \tag{16}$$

where the 0 subscript represents the bulk value. Specifically, κ_0 and D_0 refer to the ionic conductivity and diffusion coefficient in pure electrolyte ($\epsilon = 1$), and σ_0 refers to the electronic conductivity in non-porous solid ($\epsilon = 0$). Note that D_0 and κ_0 are computed from the individual ion species as

$$D_0 = D_{0_+} D_{0_-} \frac{z_+ - z_-}{z_+ D_{0_+} - z_- D_{0_-}}, \tag{17}$$

$$\kappa_0 = F^2 c(z_+^2 \nu_+ u_{0_+} + z_-^2 \nu_- u_{0_-}). \tag{18}$$

The values for bulk conductivities, i.e. σ_0 and κ_0, and porosity are readily available from experimental data. The bulk diffusion coefficient, transference number, and specific surface area are more difficult to measure.

Comparison with experimental data indicates that the Bruggeman correlation overestimates ionic conductivity in porous electrodes with certain particle arrangements (Tjaden et al, 2016, 2018). Therefore, we also consider a modified correlation that reduces ionic conductivity and diffusion coefficient inside the porous material by equating $\kappa = f_m \epsilon^{\frac{3}{2}} \kappa_0$ and $D_i = f_m \epsilon^{\frac{3}{2}} D_{0,i}$, where f_m is a correction coefficient that takes values in the range $[0.02, 0.79]$, depending on the electrode microstructure (Madabattula and Kumar, 2020).

3.2 Nondimensionalization

To facilitate the analysis, we nondimensionalize the system described by (15) by defining the dimensionless quantities:

$$
\begin{aligned}
\hat{\Phi}_1 &= \frac{F}{RT}\Phi_1, & \hat{c} &= \frac{c}{c_0}, & \hat{t} &= \frac{D_0}{L^2}t, \\
\hat{\Phi}_2 &= \frac{F}{RT}(\Phi_2 + U_0), & \hat{\mathbf{x}} &= \frac{\mathbf{x}}{L}.
\end{aligned}
\tag{19}
$$

The dimensionless location $\hat{\mathbf{x}}$ leads to the nondimensional domain $\hat{\Omega}$ and boundaries $\hat{\Gamma}_a$ and $\hat{\Gamma}_c$, as well as gradient $\hat{\nabla}$. We also introduce the dimensionless specific surface area $\hat{a}$, effective diffusion coefficient $\hat{D}$, and effective electronic conductivity $\hat{\sigma}$, which are design-dependent quantities we will describe in Sect. 3.4. Using (10) and (11) the dimensionless field equations read

$$
-\hat{\nabla}\cdot\left(\hat{\sigma}\hat{\nabla}\hat{\Phi}_1\right) = -\lambda\hat{a}\left(\delta_r\hat{i}_n + \delta_c\hat{i}_c\right) \qquad \text{in } \hat{\Omega},
\tag{20a}
$$

$$
-\hat{\nabla}\cdot\left(\hat{D}\hat{c}\hat{\nabla}\hat{\Phi}_2\right) - \left(\frac{t_+}{z_+} + \frac{t_-}{z_-}\right)\hat{\nabla}\cdot\left(\hat{D}\hat{\nabla}\hat{c}\right) \\
= (1-\lambda)\hat{a}\left(\delta_r\hat{i}_n + \delta_c\hat{i}_c\right) \quad \text{in } \hat{\Omega},
\tag{20b}
$$

$$
\frac{\partial(\epsilon\hat{c})}{\partial\hat{t}} - \hat{\nabla}\cdot(\hat{D}\hat{\nabla}\hat{c}) = \frac{z_+z_-}{t_+t_-(z_- - z_+)}(1-\lambda) \\
\hat{a}t_-\left(\delta_r\hat{i}_n + \left(\frac{dq_+}{dq} - \frac{t_+}{t_-}\frac{dq_-}{dq}\right)\delta_c\hat{i}_c\right) \quad \text{in } \hat{\Omega},
\tag{20c}
$$

subject to the boundary and initial conditions

$$
\begin{aligned}
\hat{\Phi}_1 &= 0 & &\text{on } \hat{\Gamma}_a, & &\text{(20d)} \\
\hat{\Phi}_1 &= \xi\hat{t} & &\text{on } \hat{\Gamma}_c, & &\text{(20e)} \\
\hat{\nabla}\hat{\Phi}_1\cdot\mathbf{n} &= 0 & &\text{on } \partial\hat{\Omega}\setminus(\hat{\Gamma}_a\cup\hat{\Gamma}_c), & &\text{(20f)} \\
\hat{\nabla}\hat{\Phi}_2\cdot\mathbf{n} &= 0 & &\text{on } \partial\hat{\Omega}, & &\text{(20g)} \\
\hat{\nabla}\hat{c}\cdot\mathbf{n} &= 0 & &\text{on } \partial\hat{\Omega}, & &\text{(20h)} \\
\hat{\Phi}_1(\hat{\mathbf{x}},\hat{t}=0) &= 0 & &\text{in } \hat{\Omega}, & &\text{(20i)} \\
\hat{\Phi}_2(\hat{\mathbf{x}},\hat{t}=0) &= 0 & &\text{in } \hat{\Omega}, & &\text{(20j)} \\
\hat{c}(\hat{\mathbf{x}},\hat{t}=0) &= \hat{c}_0 & &\text{in } \hat{\Omega}, & &\text{(20k)}
\end{aligned}
$$

for $\hat{t} \in (0,\hat{T}]$. In the above we introduce the dimensionless current densities

$$
\begin{aligned}
\hat{i}_n &= \hat{c}^\alpha\left[e^{\alpha(\hat{\Phi}_1 - \hat{\Phi}_2)} - e^{-\alpha(\hat{\Phi}_1 - \hat{\Phi}_2)}\right], \\
\hat{i}_c &= \hat{c}^\alpha\frac{\partial\left(\hat{\Phi}_1 - \hat{\Phi}_2\right)}{\partial\hat{t}}.
\end{aligned}
\tag{21}
$$

and dimensionless ionic conductivity $\hat{\kappa} = \hat{c}\hat{D}$.

For future reference we also introduce the independent dimensionless groups as

$$
\begin{aligned}
\delta_r &= \frac{a_0 i_0 L^2 F}{RT}\left(\frac{1}{\sigma_0} + \frac{1}{\kappa_0}\right), & t_+ &= \frac{z_+ u_+}{z_+ u_+ - z_- u_-}, \\
\delta_c &= a_0 C_d D_0\left(\frac{1}{\sigma_0} + \frac{1}{\kappa_0}\right), & \lambda &= \frac{\kappa_0}{\sigma_0 + \kappa_0}, \\
\xi &= \frac{\zeta L^2 F}{D_0 RT}.
\end{aligned}
\tag{22}
$$

with the following meanings

- δ_r and δ_c represent the ratios between the kinetic resistance and ohmic resistance, for redox kinetics and capacitive charging, respectively;
- λ is the ratio between the ionic conductivity and the total conductivity;
- t_+ denotes the transference number of cation; the anion transference number is related by $t_- = 1 - t_+$;
- ξ is the scan rate to diffusion timescale ratio.

Here, the ionic conductivity κ_0, the exchange current density i_0, and specific capacitance C_d are computed with the initial concentration c_0.

We also define $\delta = \delta_r + \delta_c$ as the ratio of total kinetic resistance and ohmic resistance, and $\gamma = \delta_r/\delta$ as the fractional contribution from the redox reaction, so that

$$
\begin{aligned}
\delta &= \frac{a_0 D_0 F}{RT}\left(\frac{1}{\sigma_0} + \frac{1}{\kappa_0}\right)\left(\frac{i_0 L^2}{D_0} + \frac{C_d RT}{F}\right), \\
\gamma &= \frac{i_0 L^2/D_0}{i_0 L^2/D_0 + C_d RT/F}.
\end{aligned}
\tag{23}
$$

Hence, γ can be varied while keeping δ constant to have different reaction compositions for the same total kinetic resistance. In the literature, the Wagner number, i.e. $1/\delta$, is often used to analyze the limiting kinetics and current distribution.

3.3 Electrode-specific electronic potential

In a full-cell model, the electronic potential only exists in the electrode regions (where $\bar{\rho} \to 1$). System (20) models $\hat{\Phi}_1$ on the entire domain Ω, by assigning the dimensionless electronic conductivity to a very small positive value in the separator region (where $\bar{\rho} \to 0$) so that $\hat{\sigma}\hat{\nabla}\hat{\Phi}_1 \approx 0$ in the electrolyte. However, because of filtering, $\bar{\rho}$ is not exactly zero the electrolyte region and hence the interpolated conductivity may not be negligible, which allows some electronic current to bypass the ionic phase, creating a short circuit between the electrodes. To minimize the short circuit effect, the optimized designs will position the electrodes far apart, so that $\bar{\rho}$ approaches zero in the center of the electrolyte region. Consequently, the

optimization produces suboptimal designs, with no possibility for creating interdigitated structures that are known to be effective (Hung et al, 2022; Long et al, 2004).

To prevent a short circuit and allow for interdigitation, we represent $\hat{\Phi}_1$ via two fields: $\hat{\Phi}_{1,a}$ in the anode and $\hat{\Phi}_{1,c}$ in the cathode and use the indicator functions from (5) to define their effective subdomains. The electronic potential equation (15a) is thus replaced by the two equations

$$-\hat{\nabla} \cdot \left(\mathcal{I}_a \hat{\sigma} \hat{\nabla} \hat{\Phi}_{1,a} \right)$$
$$= -\lambda \hat{a} \left(\delta_r \hat{i}_{n,a} + \delta_c \hat{i}_{c,a} \right) \qquad \text{in } \hat{\Omega}, \quad (24a)$$

$$-\hat{\nabla} \cdot \left(\mathcal{I}_c \hat{\sigma} \hat{\nabla} \hat{\Phi}_{1,c} \right)$$
$$= -\lambda \hat{a} \left(\delta_r \hat{i}_{n,c} + \delta_c \hat{i}_{c,c} \right) \qquad \text{in } \hat{\Omega}, \quad (24b)$$

with associated boundary conditions

$$\hat{\Phi}_{1,a} = 0 \qquad \text{on } \hat{\Gamma}_a, \qquad (24c)$$
$$\hat{\nabla} \hat{\Phi}_{1,a} \cdot \mathbf{n} = 0 \qquad \text{on } \partial\hat{\Omega} \setminus \hat{\Gamma}_a, \qquad (24d)$$
$$\hat{\Phi}_{1,c} = \xi \hat{t} \qquad \text{on } \hat{\Gamma}_c, \qquad (24e)$$
$$\hat{\nabla} \hat{\Phi}_{1,c} \cdot \mathbf{n} = 0 \qquad \text{on } \partial\hat{\Omega} \setminus \hat{\Gamma}_c, \qquad (24f)$$

where the anodic currents are computed as

$$\hat{i}_{n,a} = \mathcal{I}_a \hat{c}^\alpha \left[e^{\alpha(\hat{\Phi}_{1,a} - \hat{\Phi}_2)} - e^{-\alpha(\hat{\Phi}_{1,a} - \hat{\Phi}_2)} \right],$$
$$\hat{i}_{c,a} = \mathcal{I}_a \hat{c}^\alpha \frac{\partial \left(\hat{\Phi}_{1,a} - \hat{\Phi}_2 \right)}{\partial \hat{t}}, \qquad (25)$$

and cathodic currents $\hat{i}_{n,c}$ and $\hat{i}_{c,c}$ are computed similarly by replacing $\mathcal{I}_a$ and $\hat{\Phi}_{1,a}$ with $\mathcal{I}_c$ and $\hat{\Phi}_{1,c}$. For all other terms defined above, the total current densities are evaluated as $\hat{i}_n = \hat{i}_{n,a} + \hat{i}_{n,c}$, and $\hat{i}_c = \hat{i}_{c,a} + \hat{i}_{c,c}$, and the electronic potential as $\hat{\Phi}_1 = \mathcal{I}_a \hat{\Phi}_{1,a} + \mathcal{I}_c \hat{\Phi}_{1,c}$.

3.4 Design-dependent material parameters

In our topology optimization, the model parameters such as the porosity, the dimensionless surface area, electronic conductivity, and diffusivity, vary spatially as a function of the material indicator field $\bar{\rho}$. The porosity and dimensionless surface area are given by interpolations as

$$\epsilon = \epsilon_M + \bar{\rho}(\epsilon_N - \epsilon_M),$$
$$\hat{a} = \bar{\rho}^q, \qquad (26)$$

where ϵ_M is the porosity in the electrolyte/separator, ϵ_N is the porosity in the electrode, and $q \geq 1$ is a penalization parameter. The porosity ϵ is volume averaged while the specific area $\hat{a}$ is penalized. As such, intermediate regions where $\bar{\rho}(\hat{\mathbf{x}}) \neq \{0, 1\}$ have artificially smaller $\hat{a}$, thus reducing current densities.

Because of this, the optimized designs predominantly have $\bar{\rho}(\hat{\mathbf{x}}) = \{0, 1\}$, which approximates our original problem in (1), i.e. $\chi \approx \bar{\rho}$. Meanwhile, the dimensionless electronic conductivity $\hat{\sigma}$ and diffusion coefficients $\hat{D}$ are computed from the Bruggeman correlation (16) and interpolations

$$\hat{\sigma} = \bar{\rho}^p (1 - \epsilon_N)^{\frac{3}{2}},$$
$$\hat{D} = \epsilon_M^{\frac{3}{2}} + \bar{\rho}^p \left(\epsilon_N^{\frac{3}{2}} - \epsilon_M^{\frac{3}{2}} \right), \qquad (27)$$

where the parameter $p \geq 1$ is similarly used to penalize ionic and electronic transport in intermediate material regions. Note that ϵ_M is not involved in the interpolation for $\hat{\sigma}$ since the electrolyte has negligible electronic conductivity. For the modified Bruggeman correlation, the $\epsilon_N^{\frac{3}{2}}$ is replaced by $f_m \epsilon_N^{\frac{3}{2}}$ in the formula for $\hat{D}$. In this paper, we choose $\epsilon_M = 1$, $\epsilon_N = 0.5$, and $f_m = 0.02$. The choice of the penalization parameters p and q is discussed in Sect. 5.1.

3.5 Energy metrics

We list quantities used to construct the optimization cost and constraint functions, namely energy input, kinetic energy, and ohmic loss,

$$E_{\text{in}} = \frac{1}{\lambda} \int_0^{\hat{T}} \int_{\partial\hat{\Omega}} \hat{\sigma} \hat{\nabla} \hat{\Phi}_1 \cdot \mathbf{n} \hat{\Phi}_1 \, d\hat{s} \, d\hat{t}, \qquad (28a)$$

$$E_{\text{kin}} = \delta_r \int_0^{\hat{T}} \int_{\hat{\Omega}} \hat{a} \hat{i}_n (\hat{\Phi}_1 - \hat{\Phi}_2) \, d\hat{x} \, d\hat{t}$$
$$+ \delta_c \int_0^{\hat{T}} \int_{\hat{\Omega}} \hat{a} \hat{i}_c (\hat{\Phi}_1 - \hat{\Phi}_2) \, d\hat{x} \, d\hat{t}, \qquad (28b)$$

$$E_{\text{ohm}} = \frac{1}{\lambda} \int_0^{\hat{T}} \int_{\hat{\Omega}} \hat{\sigma} \hat{\nabla} \hat{\Phi}_1 \cdot \hat{\nabla} \hat{\Phi}_1 \, d\hat{x} \, d\hat{t}$$
$$+ \frac{1}{1 - \lambda} \int_0^{\hat{T}} \int_{\hat{\Omega}} \hat{D} \hat{c} \hat{\nabla} \hat{\Phi}_2 \cdot \hat{\nabla} \hat{\Phi}_2 \, d\hat{x} \, d\hat{t}$$
$$+ \frac{1}{1 - \lambda} \left(\frac{t_+}{z_+} + \frac{t_-}{z_-} \right) \int_0^{\hat{T}} \int_{\hat{\Omega}} \hat{D} \hat{\nabla} \hat{c} \cdot \hat{\nabla} \hat{\Phi}_2 \, d\hat{x} \, d\hat{t}. \qquad (28c)$$

The detailed derivation of these expressions is presented in Appendix A. The kinetic energy, henceforth referred to as the stored energy, includes both the energy stored in the chemical reaction and the dissipation due to finite charge-transfer kinetics. The energy storage depends on the thermodynamic potential, which is characteristic of a specific material system. To keep the analysis general, we do not specify the thermodynamic potential and instead infer its value via the dimensionless ionic potential, which naturally groups kinetic loss with kinetic storage.

The optimization problem focuses on reducing the ohmic losses, because this can be lowered by shaping

the electrodes to facilitate ion and electron transport across the cell. By reducing the ohmic losses, a larger current output can be extracted from the cell, for a given applied voltage. While a larger current also causes larger kinetic losses (due to the activation barrier for redox reaction) we expect the cell efficiency to be dominated by transport losses.

4 Implementation

We resolve the governing equations (20), (24), filtering equation (2), and boundary propagation equation (4) with the finite element library `Firedrake` (Ham et al, 2023), which uses `PETSc` (Balay et al, 2023a,b) as the backend for the iterative solvers. The sensitivities of the optimization cost and constraint functions are computed by `pyadjoint` (Mitusch et al, 2019). A `Python` implementation of the MMA algorithm (Svanberg, 1987), `pyMMAopt` (Salazar de Troya, 2021) is used to solve the optimization problem. The designs are considered converged after 350 iterations, where the change in the normalized objective function is typically in the magnitude of 10^{-3}.

Piecewise linear finite elements are used for spatial discretization of the governing physics equations (20) and (24). We use a mixed finite element method to solve the filtering equation (2) and the continuous boundary propagation problem (4), as detailed in Appendix B. The domain is either partitioned into triangular (2D) or tetrahedral (3D) elements. The two-dimensional domain is a rectangle with distance between the current collectors of nondimensional length 1 and the width of 2. The additional dimension of the three-dimensional domain is a depth of 2. We simulate half of the total domain in 2D, and a quarter in 3D, due to the domain symmetry. The total number of degrees of freedom (DoF) for 2D and 3D models are ∼60k and ∼4M, respectively. Backward Euler is used for temporal discretization with 20 total timesteps for a dimensionless simulation time of 1, which is the smallest number of timesteps that is stable for all studies. We parallelize the computation via an approximately 20k DoFs/CPU load.

With a transient problem, computing sensitivities with the adjoint method requires storing the primal response for all timesteps. In this work, we have not encountered any memory bottleneck, but it is an inevitability for larger simulations. In response, checkpointing schemes such as Griewank and Walther (2000) can be utilized.

The finite element system corresponding to (20) with the two-electronic potential formulation (24) is solved using Newton's method with linesearch. The 2D linearized systems are solved using a direct method. For the 3D cases, however, an iterative method with
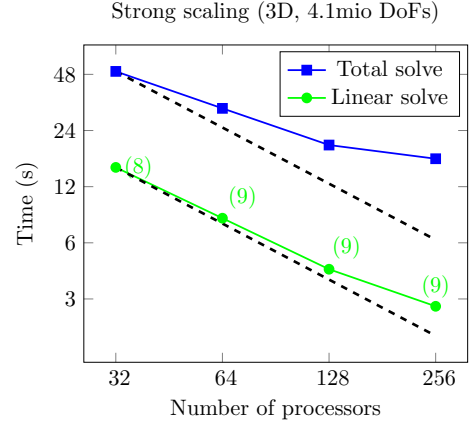

Fig. 4: Strong scaling for the 3D solver. The timings show the total solution time and the total linear solver time where the number of GMRES iterations appears in the parentheses.

a scalable preconditioner is essential (Wathen, 2015). The linearized systems have the following block form:

$$\begin{bmatrix} A_{11} & A_{12} & A_{13} & A_{14} \\ A_{21} & A_{22} & A_{23} & A_{24} \\ A_{31} & A_{32} & A_{33} & A_{34} \\ A_{41} & A_{42} & A_{43} & A_{44} \end{bmatrix} \begin{bmatrix} \Delta\boldsymbol{\Phi}_{1,\mathrm{c}} \\ \Delta\boldsymbol{\Phi}_{1,\mathrm{a}} \\ \Delta\boldsymbol{\Phi}_2 \\ \Delta\mathbf{c} \end{bmatrix} = \begin{bmatrix} \mathbf{r}_1 \\ \mathbf{r}_2 \\ \mathbf{r}_3 \\ \mathbf{r}_4 \end{bmatrix}, \quad (29)$$

where $\mathbf{r}_i$, $i \in \{1,2,3,4\}$, are the residual vectors corresponding to Eqn. (24b), (24a), (20b), and (20c) that are expressed in terms of the $j \in \{1,2,3,4\}$ response vectors $\Delta\boldsymbol{\Phi}_{1,c}$, $\Delta\boldsymbol{\Phi}_{1,a}$, $\Delta\boldsymbol{\Phi}_2$, and $\mathbf{c}$. Each block A_{ij} represents the linearization of the finite element residual $\mathbf{r}_i$ with respect to vector j.

The diagonal blocks A_{ii} result from the discretization of elliptic or parabolic operators, for which multigrid methods (Brandt, 1977) are often ideal preconditioners. We thus use the preconditioned GMRES (Saad and Schultz, 1986), with a block triangular preconditioner of the form

$$P = \begin{bmatrix} A_{11} & 0 & 0 & 0 \\ A_{21} & A_{22} & 0 & 0 \\ A_{31} & A_{32} & A_{33} & 0 \\ A_{41} & A_{42} & A_{43} & A_{44} \end{bmatrix}. \quad (30)$$

Evaluating the inverse of this matrix requires the inverses of the diagonal blocks A_{ii}, which is done approximately using a single AMG V-cycle (Ruge and Stüben, 1987) `BoomerAMG` (Henson and Yang, 2002) from the `hypre` library (Falgout and Yang, 2002). The `PETSc` options for solving the field equations, the filter problem, and boundary propagation problem can be found in Appendix C.

In Fig. 4, we investigate the scalability of this preconditioning approach. For this investigation, we simulate the first timestep for the initial uniform $\rho =$

0.5 design. We observe that the linear solver of (29) exhibits almost linear scalability, which indicates that our preconditioning is effective.

5 Results and discussion

Herein, we introduce the optimization strategy and optimize designs for various choices of dimensionless parameters. The fixed dimensionless parameters among all designs are listed in Table 1. Table 2 lists

Table 1: Dimensionless parameters that are **fixed** amongst all designs.

Parameter	Quantity	Value
α	charge transfer coefficient	0.5
t_+	cation transference number	0.5
ξ	potential scan rate	1.0
$\hat{T}$	final time	1.0
ϵ_M	electrolyte porosity	1.0
ϵ_N	electrode porosity	0.5

the three dimensionless parameters that are varied amongst the designs. The results presented in Sect. 5.2 show how different combinations of $(\lambda, \delta, \gamma)$ lead to different optimal electrode designs.

5.1 Optimization problem setup

In this section, we introduce several strategies devised to improve the convergence and effectiveness of the optimization algorithm. Given the complexity of the physical problem, we need to carefully define the cost and constraint functions and the initial design in order to effectively traverse the design space and find optimized designs.

5.1.1 Parameter penalizations

To promote binary $\bar{\rho}(\hat{\mathbf{x}}) \approx \{0, 1\}$ designs, we use different interpolations for the design-dependent quantities $\hat{a}$, $\hat{\sigma}$, and $\hat{D}$ in the cost and constraint functions, as compared to the primal model, cf. (20) and (24) in

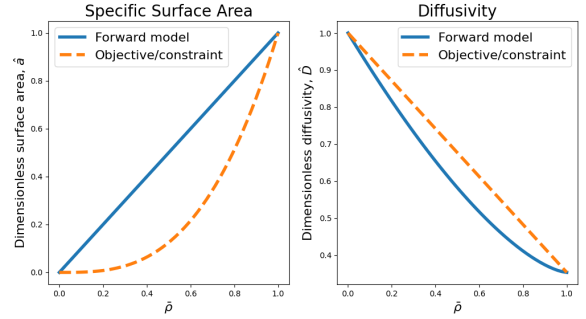Sect. 3.4. In the cost and constraint computations, $\hat{a}$ is

Fig. 5: Different penalization for specific surface area and ionic conductivity for the primal analysis and cost/constraint computation to produce binary designs.

interpolated with $q = 3$, whereas in the primal analysis $q = 1$, cf. (26). Reversely, $\hat{\sigma}$ and $\hat{D}$ use $p = 1$ in the cost and constraint computations and $p = 1.5$ in the primal analysis. The different interpolations adopted for the primal analysis and the cost/constraint computations are visualized in Fig. 5. The $q = 3$ penalization for the specific surface area and $p = 1.5$ for the conductivity disproportionately reduces the energy storage and disproportionately increases the ohmic loss in the intermediate material regions. These penalizations lead to inefficient use of intermediate material regions and hence the size of such regions in the optimized designs is small.

5.1.2 Cost and Constraint

Maximizing the kinetic energy E_{kin} defined in (28) is an intuitive choice for the (negative) cost function, as a proxy for maximizing energy stored. Unfortunately, this choice does not consider the ohmic loss. Most importantly, this cost function would not benefit from the (27) diffusivity/conductivity interpolation scheme. In response, we formulate the optimization problem as follows

$$\max_{\rho:\, \Omega \to [0,1]} \theta_0 = \frac{1}{2} \left(E_{\text{kin}} + E_{\text{in}} - E_{\text{ohm}} \right)$$

$$\text{subject to } \theta_1 = \frac{E_{\text{ohm}}}{E_{\text{in}}} \leq \eta_{\max}, \quad (31)$$

i.e. we maximize energy storage and ensure a minimum energy efficiency of $(1 - \eta_{\max})$. According to (31), the design can be optimized by either increasing E_{kin} or decreasing E_{ohm}. And hence the interpolations of $\hat{a}$, $\hat{\sigma}$, and $\hat{D}$ produce disproportionately lower E_{kin} and disproportionately higher E_{ohm} from the intermediate material regions for the cost and constraint functions,

---

Table 2: Dimensionless parameters that are **varied** amongst the designs.

Parameter	Quantity
λ	ratio between ionic and total conductivity
δ	ratio between ohmic and kinetic resistance
γ	redox contribution to total reaction

relative to the primal analysis. As such the optimizer generates predominantly $0 - 1$ designs.
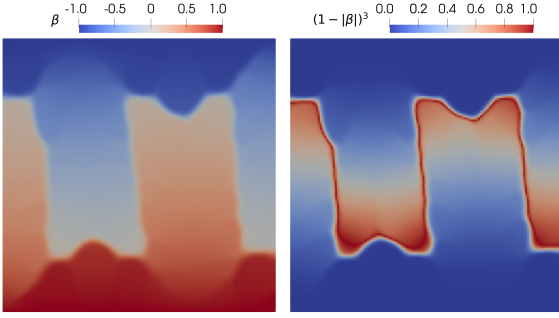

Fig. 6: Interdigitated electrodes with near uniform $\beta \approx \pm 1$ distribution bounded by a thin separator layer with large $(1 - |\beta|)^3$ values.

According to (24), the only relation between the two electronic potentials is through the reaction terms. Consequently, a physical connection between the anode and cathode is not simulated as a short circuit (electronic current bypassing the reaction). To prevent such connections, we define the short circuit intensity

$$\mathcal{I}_{\mathrm{SC}} = \int_{\Omega} (1 - |\beta|)^3 \, \bar{\rho} \, \mathrm{d}\hat{x} \qquad (32)$$

The term $(1 - |\beta|)^3$ takes its maximum value when $\beta = 0$. In the absence of a short circuit, in the electrodes where $\bar{\rho} \approx 1$, we have a near uniform $\beta = \pm 1$ distribution. The exception occurs in the separator layer where β experiences a sharp transition as illustrated in Fig. 6. A "small" short circuit intensity requires $\bar{\rho} \approx 0$ when $\beta \neq \pm 1$, thus ensuring the electrolyte fills the gap between the electrodes. We weakly enforce this short circuit intensity constraint via the penalty method, i.e. we now solve the optimization problem

$$\min_{\rho \colon \Omega \to [0,1]} \tilde{\theta}_0 = \frac{1}{\theta_0} + w_{\mathrm{SC}} \mathcal{I}_{\mathrm{SC}}$$

$$\text{subject to } \theta_1 = \frac{E_{\mathrm{ohm}}}{E_{\mathrm{in}}} \leq \eta_{\max}, \quad (33)$$

where $w_{\mathrm{SC}} = 1$ is the penalty weight used in our study. Note that the minimization of $-\theta_0$, is less robust than $\frac{1}{\theta_0}$ since it requires case-specific scaling values for θ_0. However, in order for (33) to work properly, $E_{\mathrm{ohm}} < E_{\mathrm{in}} + E_{\mathrm{kin}}$ must be satisfied at initial design, so that the cost $\tilde{\theta}_0$ is always positive, and hence minimized by maximizing θ_0. If $\theta_0 < 0$, then $\tilde{\theta}_0$ is minimized as $\theta_0 \to 0^-$, which completely changes the optimization trajectory and hence designs.

It is well known that the optimized designs may depend on the initial design. To this end, we solve the optimization problem using three uniform initial designs $\rho(\mathbf{x}) \in \{0.45, 0.5, 0.55\}$ and choose the best overall design. Let $\theta_1^{(0)}$ denote the ohmic loss ratio of the initial design. We set the constraint bound $\eta_{\max} = \theta_1^{(0)} * \Sigma$, where $\Sigma \in (0.0, 1.0]$. We generate designs for different combinations of dimensionless parameters, with both original and modified Bruggeman correlation. $\Sigma = 0.4$ is used for all $\delta = 0.5$, $\lambda = 0.1$, and the three-dimensional designs; $\Sigma = 0.5$ is used for all other designs.

A typical optimization convergence history is illustrated in Fig. 7. During early design iterations, the constraint drives the optimization to satisfy the $\theta_1 \leq \eta_{\max}$ constraint by separating the electrodes. Also, more electrode material leads to additional reaction current and increased ohmic loss. Because of this, the constraint limits the maximum amount of electrode material and thus prevents short circuits from appearing in the design as the optimization continues. While eliminating short circuits is necessary, a tight constraint hinders the development of structures as the optimization continues. Therefore, we deactivate this constraint after the bulk design features have formed, which for our study is after iteration 150. The ensuing iterations refine the shape rather than the overall layout. To summarize, Σ strongly affects the optimization during early iterations to find the interdigitation topology but it has no effect during later iterations.

5.1.3 Case specific treatments

Certain cases within our parameter sweep require extra care. 1) For cases with the original Bruggeman correlation, i.e. $f_m = 1$, large effective ionic conductivity/diffusivity within the porous electrode allows ions to travel deeper into the pore network, resulting in better material utilization as discussed in Sect. 5.3. Accordingly, during early design iterations, the optimizer positions a considerable amount of electrode material in the middle region to benefit from the largest potential drop. Unfortunately this causes a strong connection between the electrodes that cannot be removed in the later design iterations. To remedy this, the optimization adopts a continuation strategy wherein the initial design uses the modified Bruggemann correlation with $f_m = 0.02$ which increases to the target $f_m = 1$ after iteration 50. 2) For cases with large δ, we observe $\theta_0 < 0$ from the initial design, which is undesirable as stated above. We remedy this by invoking yet another continuation strategy where the initial design uses a smaller δ such that $E_{\mathrm{ohm}} < E_{\mathrm{in}} + E_{\mathrm{kin}}$ is satisfied. In our study, the $\delta = 5$ cases start with $\delta = 2$ and increase to its target value after iteration 50 (see Fig. 7).
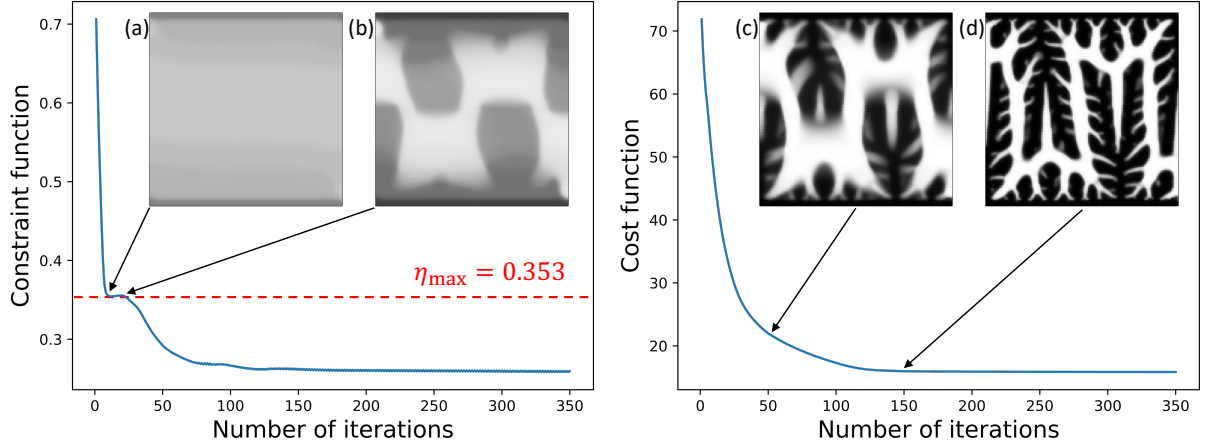
Fig. 7: Cost and constraint function history for $\delta = 2, \gamma = 0.5, \lambda = 0.01$ with modified Bruggeman correlation. The inserts are the designs at iteration (a) 8, (b) 20, (c) 50, and (d) 150. Only one symmetric half of the design is illustrated to save space.

In some extreme situations, namely the $\delta = 5$ with modified Bruggeman correlation cases, large regions of intermediate material appear in the optimized designs. The small values for E_{kin} and E_{ohm} in these regions are overshadowed by the other regions where the current density is substantial. As such, the penalization scheme is not effective. To counter this effect, we scale E_{kin} and E_{ohm} after the bulk structures are established (i.e. after iteration 150 when the efficiency constraint is deactivated). To motivate our scaling scheme, refer to the typical β distribution shown in Fig. 3 (right-hand side) where $|\beta| \approx 0$ around the electrode tips and $|\beta| \approx 1$ near the current collectors. Accordingly, we consider three different types of scaling, namely $|\beta|$, $1 - |\beta|$, and $|\beta|(1 - |\beta|)$, to scale down the energy integrands around the electrode tip, the current collector, and both, respectively. The scaling is readily incorporated into our strategy with a continuation scheme. With $|\beta|$ scaling as an example, the energy storage is computed by

$$\tilde{E}_{\text{kin}} = \delta_r \int_0^{\hat{T}} \int_{\hat{\Omega}} |\beta|^s \hat{a} \hat{i}_n (\hat{\Phi}_1 - \hat{\Phi}_2) \, d\hat{x} \, d\hat{t}$$
$$+ \frac{\delta_c}{2} \int_{\hat{\Omega}} |\beta|^s \hat{a} (\hat{\Phi}_1 - \hat{\Phi}_2)^2 \, d\hat{x}, \quad (34)$$

where $s = 0$ for the first 150 iterations where after it is increased to $s = 1$. We use the $|\beta|$ scaling for E_{kin} and E_{ohm} in the $\gamma = \{0.5, 1\}$ cases. For the $\gamma = 0$ case, we use $|\beta|$ scaling for E_{kin} and $|\beta|(1 - |\beta|)$ scaling for E_{ohm}.

For the 3D optimization case, a slight connection of the electrodes appears near a wall. Some of the strategies described above could be used to prevent

this short circuit design: different initial designs, scaling, etc. Instead, motivated by Lazarov et al (2016), we implement a simple dilation/erosion strategy, which allows us to remove the short circuit. This strategy applies a one-time adjustment to the design field ρ, which is localized to the connection region. Namely, we use shifted versions of the electrode indicator functions (5) such that

$$\tilde{\mathcal{I}}_a = H_{100,0.52}\left(\frac{\beta + 1}{2}\right),$$
$$\tilde{\mathcal{I}}_c = H_{100,0.52}\left(\frac{-\beta + 1}{2}\right). \quad (35)$$

In this way, regions where $\tilde{\mathcal{I}}_a = 1$ and $\tilde{\mathcal{I}}_c = 1$ are reduced in size as compared to $\mathcal{I}_a$ and $\mathcal{I}_c$ computed by $H_{100,0.5}$. Then there exists a subdomain Ω_s such that $\tilde{\mathcal{I}}_a(\mathbf{x}) + \tilde{\mathcal{I}}_c(\mathbf{x}) = 0$ for all $\mathbf{x} \in \Omega_s$. Subsequently we equate $\rho := \rho(\tilde{\mathcal{I}}_a + \tilde{\mathcal{I}}_c)$ to ensure $\rho = 0$ in Ω_s. Once the connection is removed, it is unlikely to reconnect due to the short circuit intensity penalization. We perform the shifted indicator adjustment after iteration 150. Note that the remaining iterations are still completed with the original indicator functions $\mathcal{I}_a$ and $\mathcal{I}_c$. This disconnection strategy is only appropriate when the electrode connections are of a small "grazing" type, and if so, has very little effect on the trajectory of the optimization. Meanwhile, "head-on collision" connections should be avoided earlier in the optimization using strategies mentioned above.

5.2 Discussion of generated designs

We generate optimized designs with various combinations of the dimensionless parameters δ, λ, and γ.

We choose energy storage and ohmic loss as performance metrics and compare the optimized designs to a monolithic design with electrode separation distance of 0.05, as this is the average gap among all optimized designs. The optimized designs are shown in Fig. 8 - 12 with the percentage improvement over the monolithic design. In the following subsections, we discuss the designs corresponding to various combinations of the three nondimensional parameters listed in Table 2, and Bruggeman correlation functions (which approximates the tortuosity of the ion-diffusion pathway within the porous electrodes.)

Here, λ, i.e. the ratio between ionic and total conductivity (defined in (22)), affects the macroscale localization of the reaction front. In cases where ionic conductivity is limiting ($\lambda < 0.5$), the reaction front localizes at the electrode/separator interface. Conversely, when the electronic conductivity is the limiting factor, ($\lambda > 0.5$), the reaction front shifts towards the current collector.

The parameter δ, i.e. the ratio between ohmic and kinetic resistance (defined in (22)), controls the electrode penetration depth. In the absence of concentration gradients, the relative reaction rate between the back and the front of electrodes can be quantified by (Fuller and Harb, 2018)

$$\text{Relative rate} \approx \frac{1}{\cosh\left(\sqrt{\delta}\right)}. \tag{36}$$

For small δ values, the system is dominated by the kinetic resistance, and results in a uniform or near-uniform distribution of current density, which leads to a uniform reaction throughout the electrode. In this case, the macroscale geometry of the electrode has less effect on the electrode material utilization, i.e. monolithic designs perform sufficiently well. On the other hand, for large δ values, the system is dominated by ohmic resistance and results in a non-uniform (localized) distribution of current density. As mentioned in the introduction, thick monolothic electrodes perform poorly due to small penetration depth. Therefore, this case favors designs with complex electrode geometries.

5.2.1 Original Bruggeman correlation

Shown in Fig. 8 is the first series of designs generated using the original Bruggeman correlation, a fixed $\lambda = 0.01$, and varying δ and γ. All optimized designs possess an interdigitated structure, which was found by the optimization algorithm thanks to the continuation schemes described in Sect. 5.1. The interdigitation allows reactions to happen closer to the current collectors, boosting current density. The structure also reduces ohmic losses by promoting more efficient ionic transport. It is important to note that, if we simply force electrode separation by increasing the weight

w_{SC} on the short circuit intensity penalty in (33), we obtain near monolithic designs with a large distance between electrodes.

The first benefit of interdigitation is a more uniform concentration distribution. We quantify the concentration variation by

$$\hat{c}_{\text{var}} = |\hat{\Omega}|^{-\frac{1}{2}} \|\hat{c} - \bar{c}\|_{L^2(\hat{\Omega})}, \tag{37}$$

where $\bar{c} = 1$ is the average dimensionless concentration in the system. As illustrated in Fig. 9, using the $\delta = 5$ and $\gamma = 1$ case as an example, the interdigitated design decreases the variation in concentration by more than 50% over the monolithic design. A more uniform concentration distribution ensures better ion adsorption and redox reaction, since small concentrations hinder the adsorption/reaction rate, while large localized concentrations indicate poor ion utilization.

In the case of redox-active materials ($\gamma = 1$), the interdigitation also increases the electrode area in contact with the pure electrolyte region, facilitating ion transport between electrolyte and electrode regions. For an applied voltage boundary condition, interdigitation reduces the cell resistance and hence increases the current output. Summarizing, by facilitating ion transport in the electrolyte, the interdigitated design reduces the energy dissipation and improves cell efficiency.

For small λ, energy dissipation mainly results from ion transport and is proportional to the magnitude of the ionic-potential gradient. We compute the average gradient magnitude of ionic potential by

$$|\hat{\nabla}\hat{\Phi}_2|_{\text{avg}} = |\hat{\Omega}|^{-1}\|\hat{\nabla}\hat{\Phi}_2\|_{L^2(\hat{\Omega})}. \tag{38}$$

Fig. 9 shows a more uniform ionic potential distribution in the optimized design compared to that in the monolithic design, and a 40% decrease in the average gradient.

In kinetic resistance limited cases ($\delta = 0.5$), there are no notable differences between the designs obtained with different γ values (see left column in Fig. 8.). In other words, the bulk geometry is not sensitive to the partitioning between capacitive and redox reaction due to reactions being more uniform. Indeed, the designs are driven by the heterogeneous ohmic losses E_{ohm}. In these cases, the interdigitated optimized designs achieve a maximum energy storage increase of 10%, and a maximum ohmic loss decrease of 60% over the monolithic design.

For the ohmic resistance limited cases ($\delta = 5$), we notice obvious variations among the designs (see the right column in Fig. 8). The periodicity of the designs remains the same for varying γ values. Since the current model does not incorporate surface concentration that limits the maximum ion adsorption, the overall concentration decreases significantly for capacitor electrodes. Therefore, for capacitive-dominated
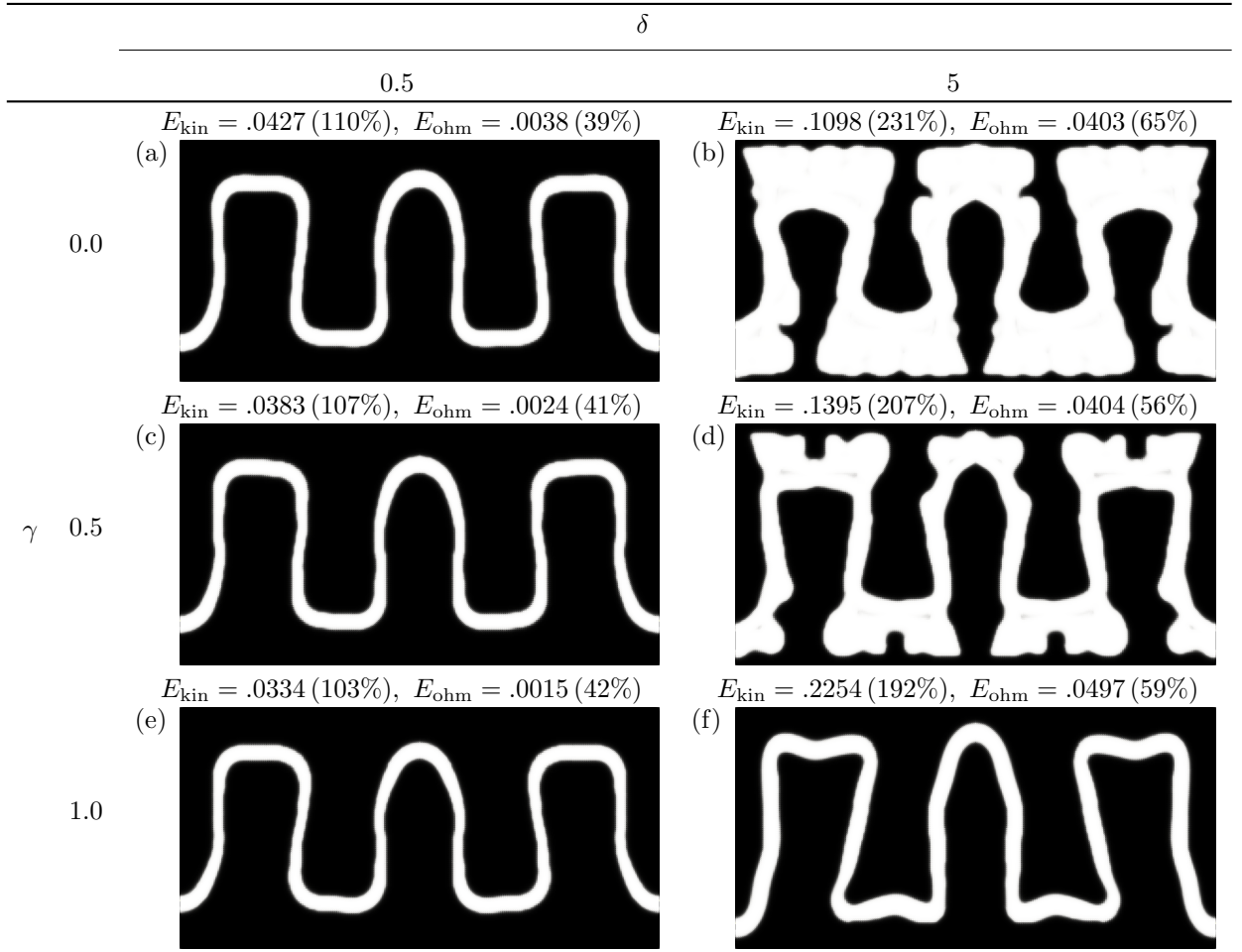
	δ	
	0.5	5

Fig. 8: Optimized porous electrode designs modeled with the original Bruggeman correlation, $\lambda = 0.01$, and varying δ/γ. Black is $\bar{\rho} = 1$; white is $\bar{\rho} = 0$.

reactions (small γ), more electrolyte is needed to support the reaction and prevent reactant starvation and dramatic energy dissipation. This explains the wider white separation region between the electrodes in the $\gamma = 0$ design. As the charging becomes more redox dominated ($\gamma \to 1$), the designs' interdigitation depth increases, reducing the separation distance between the electrodes. Such an effect is only obvious in these ohmic resistance limited cases. A smaller separation distance results in a faster ion exchange between the electrodes and hence sustains high reaction rates. Additionally, more electrode material is placed close to the current collectors to support the reaction on the electrode tips. For these $\delta = 5$ designs, we observe approximately 100% increase in energy storage and 40% reduction in ohmic loss over the monolithic design.

Next, we study the effect of varying λ and γ for a fixed $\delta = 2$. A small λ indicates larger relative electronic conductivity, which benefits designs with more intensive interdigitation. A small λ is characteristic of Graphite-based anodes with large electronic conductivity, in the order of $1000\,\mathrm{mS/cm}$, and in porous cathodes that incorporate carbon additives to enhance the average electric conductivity. On the other hand, the average room-temperature conductivity of liquid electrolyte materials is on the order of $10\,\mathrm{mS/cm}$. Overall, it is reasonable to assume that the electronic conductivity is at least one or two orders of magnitude larger than the ionic conductivity. This corresponds to λ values ranging from 0.01 to 0.1.

As shown in Fig. 10, we observe long and bulky columns in the $\lambda = 0.01$ designs. These designs achieve substantial current densities over the electrode tip due to the larger over-potential. The ohmic loss associated
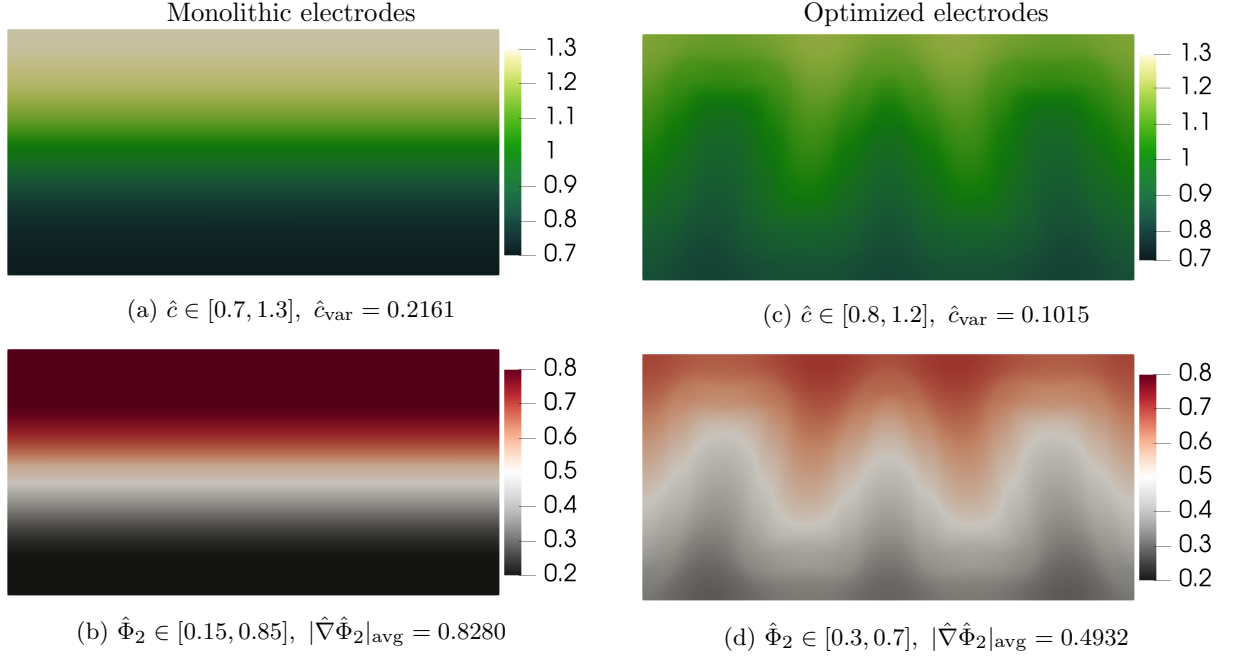
Monolithic electrodes

(a) $\hat{c} \in [0.7, 1.3]$, $\hat{c}_{\mathrm{var}} = 0.2161$

Optimized electrodes

(c) $\hat{c} \in [0.8, 1.2]$, $\hat{c}_{\mathrm{var}} = 0.1015$

(b) $\hat{\Phi}_2 \in [0.15, 0.85]$, $|\hat{\nabla}\hat{\Phi}_2|_{\mathrm{avg}} = 0.8280$

(d) $\hat{\Phi}_2 \in [0.3, 0.7]$, $|\hat{\nabla}\hat{\Phi}_2|_{\mathrm{avg}} = 0.4932$

Fig. 9: Concentration (top) and ionic potential (bottom) distributions of monolithic and optimized electrodes with $\delta = 5$, $\gamma = 1$, $\lambda = 0.01$, and the original Bruggeman correlation.

with transporting the electrons to and from the current collector is negligible, and thus results in more efficient designs.

Comparing the $\lambda = 0.1$ cases (right column in Fig. 10) with the $\lambda = 0.01$ cases (left column in Fig. 10), we notice that an increase in λ favors designs with more complexity. This can be attributed to the fact that as λ approaches 0.5, electron and ion transport become equally limiting. Consequently, smaller electrode columns are needed to shorten electron transport distance. This explain why the designs have more thinner columns. And unlike the sharp teeth-like structures observed in Roy et al (2022), the features here have round corners since smaller curvature enhances ion diffusion, and prevents electric field congestion. Deep interdigitation provides smaller benefits as compared to the previous cases. However, maximizing the interfacial area with the pure electrolyte region is still desirable as it introduces additional pathways for ionic current to enter and leave the pure electrolyte region. Therefore, the complex bulk geometry enhances the ionic transport within the porous electrode region, and thus reduces local ion depletion.

The optimization mainly tries to reduce energy dissipated due to ohmic resistance in these $\delta = 2$ designs. Therefore, the $\lambda = 0.1$ designs with increased electronic resistance generally store less energy. Although all optimized designs outperform the

monolithic design, the designs generated with $\lambda = 0.01$ provide an additional 40% increase in energy storage and 30% reduction in ohmic loss, as compared to the corresponding $\lambda = 0.1$ cases.

5.2.2 Modified Bruggeman correlation

We now compare the results generated using the modified Bruggeman correlation with $f_m = 0.02$, which is equivalent to reducing ionic diffusion inside the porous electrode by 50 times. As a result, the penetration depth of the reaction front in the monolithic design is further diminished. We first compare the designs from different reaction regimes. The results are shown in Fig. 11. To compensate for extremely slow ionic diffusion inside the electrode phase, all designs form spikey teeth-like structures to increase the interfacial area with the pure electrolyte.

Similar to the observations made from the original Bruggeman cases, among the $\delta = 0.5$ designs, changing γ does not noticeably change the design because it does not improve the uniformity of current distribution. For the $\delta = 5$ designs, capacitor electrodes ($\gamma = 0$) are thinner with shorter spikes as compared to redox electrodes ($\gamma = 1$) due to the depletion of ions in the electrolyte that causes substantial increases in ohmic loss.

By increasing δ (see right column of Fig. 11), we observe a marked increase in the number of spikes and
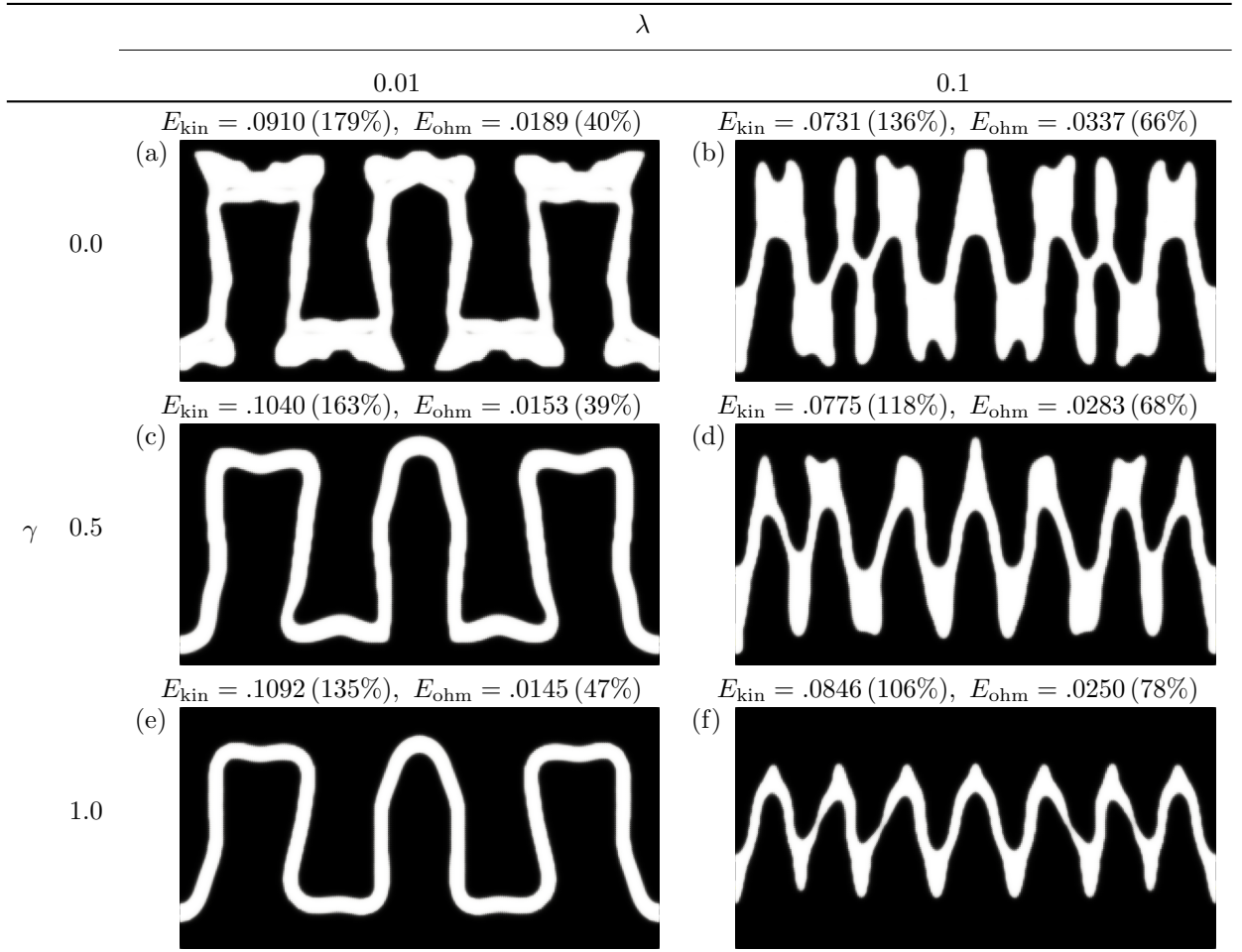
	λ	
	0.01	0.1

$E_{\text{kin}} = .0910\,(179\%),\ E_{\text{ohm}} = .0189\,(40\%)$ $E_{\text{kin}} = .0731\,(136\%),\ E_{\text{ohm}} = .0337\,(66\%)$

(a)   0.0   (b)

$E_{\text{kin}} = .1040\,(163\%),\ E_{\text{ohm}} = .0153\,(39\%)$ $E_{\text{kin}} = .0775\,(118\%),\ E_{\text{ohm}} = .0283\,(68\%)$

(c) γ 0.5   (d)

$E_{\text{kin}} = .1092\,(135\%),\ E_{\text{ohm}} = .0145\,(47\%)$ $E_{\text{kin}} = .0846\,(106\%),\ E_{\text{ohm}} = .0250\,(78\%)$

(e)   1.0   (f)

Fig. 10: Optimized porous electrode designs modeled with the original Bruggeman correlation, $\delta = 2$, and varying λ/γ. Black is $\bar{\rho} = 1$; white is $\bar{\rho} = 0$.

the teeth features protrude deeper into the electrode columns. The limiting kinetics of localized reactions is compensated by the increased interfacial area with the pure electrolyte region, allowing for better ion transport.

Conversely, in monolithic designs, electrode utilization is poor. Charging occurs only in the regions immediately adjacent to the electrolyte interface, leading to minimal energy storage, as further discussed in Sect. 5.3. Therefore, we observe exceptional improvements on energy storage across all cases, ranging from 350% to 750%. And despite significantly larger charging currents, the ohmic loss is only increased by a maximum of 200%. Considering that the energy input is much larger due to a lower overall cell resistance, the energy efficiency for the optimized designs improves significantly.

The second group of results obtained with the modified Bruggeman correlation is illustrated in Fig. 12 for two values of λ. Similar to the observations made in the corresponding original Bruggeman designs (Fig. 10), going from $\lambda = 0.01$ to $\lambda = 0.1$, the design complexity increases. Interestingly, the frequency of the microscale teeth remains roughly the same between the $\lambda = 0.01$ and $\lambda = 0.1$ designs with the same γ. The teeth in the $\lambda = 0.01$ designs are enlarged proportionally with the macroscopic structures. We observe 500% to 750% improvement in energy storage with only $\sim 50\%$ increase in ohmic loss.

5.2.3 Summary

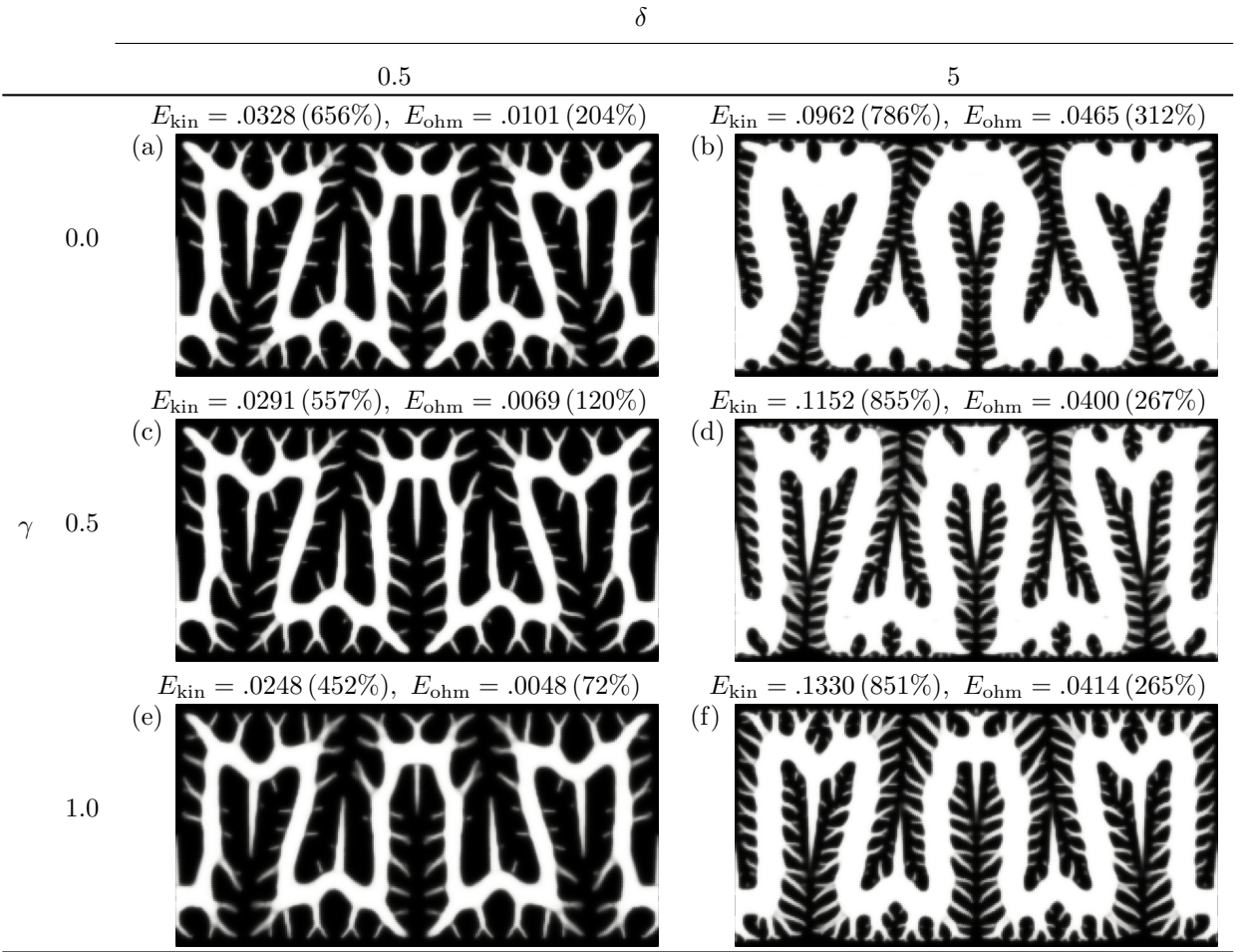To summarize the effect of different dimensionless groups on the performance and optimized design:

	δ	
	0.5	5

$E_{\mathrm{kin}} = .0328\,(656\%),\ E_{\mathrm{ohm}} = .0101\,(204\%)$ $E_{\mathrm{kin}} = .0962\,(786\%),\ E_{\mathrm{ohm}} = .0465\,(312\%)$

(a)   (b)

γ = 0.0

$E_{\mathrm{kin}} = .0291\,(557\%),\ E_{\mathrm{ohm}} = .0069\,(120\%)$ $E_{\mathrm{kin}} = .1152\,(855\%),\ E_{\mathrm{ohm}} = .0400\,(267\%)$

(c)   (d)

γ 0.5

$E_{\mathrm{kin}} = .0248\,(452\%),\ E_{\mathrm{ohm}} = .0048\,(72\%)$ $E_{\mathrm{kin}} = .1330\,(851\%),\ E_{\mathrm{ohm}} = .0414\,(265\%)$

(e)   (f)

1.0

Fig. 11: Optimized porous electrode designs modeled with the modified Bruggeman correlation, $\lambda = 0.01$, and varying δ/γ. Black is $\bar{\rho} = 1$; white is $\bar{\rho} = 0$.

- The energy gain is more significant in systems limited by ohmic resistance (mainly mass transport induced resistance), corresponding to large δ values, with δ being the inverse Wagner number.
- Macroscale features are most effective in enhancing overall ionic transport for porous electrodes that have high electronic conductivity corresponding to small λ values.
- In extreme tortuosity systems characterized by the modified Bruggeman case, features with spikey teeth are advantageous because they provide secondary paths for ion transport.
- Interdigitated electrodes reduce the transport distance and increase active-material utilization.

5.3 Performance improvements

In this section, we compare the energy storage and ohmic loss between the optimized and monolithic designs to illustrate the improved material utilization and ionic transport of the optimized cells. The material utilization is quantified by the normalized variation in energy storage density

$$E_{\mathrm{var}} = \left\| \bar{\rho} \left(\frac{E(\hat{x})}{\bar{E}} - 1 \right) \right\|_{L^2(\hat{\Omega})}, \tag{39}$$

where

$$\bar{E} = \left(\int_{\Omega} \bar{\rho}\, \mathrm{d}\hat{x} \right)^{-1} E_{\mathrm{kin}} \tag{40}$$

is the average energy density. The effectiveness of ionic transport is quantified by the average cell resistance

$$R_{\mathrm{avg}} = \hat{T}^{-1} \int_0^{\hat{T}} \frac{\xi \hat{t}}{\int_{\hat{\Gamma}_c} \hat{\sigma} \hat{\nabla} \cdot \hat{\Phi}_1 \cdot \mathbf{n}\, \mathrm{d}\hat{x}}\, \mathrm{d}\hat{t}. \tag{41}$$
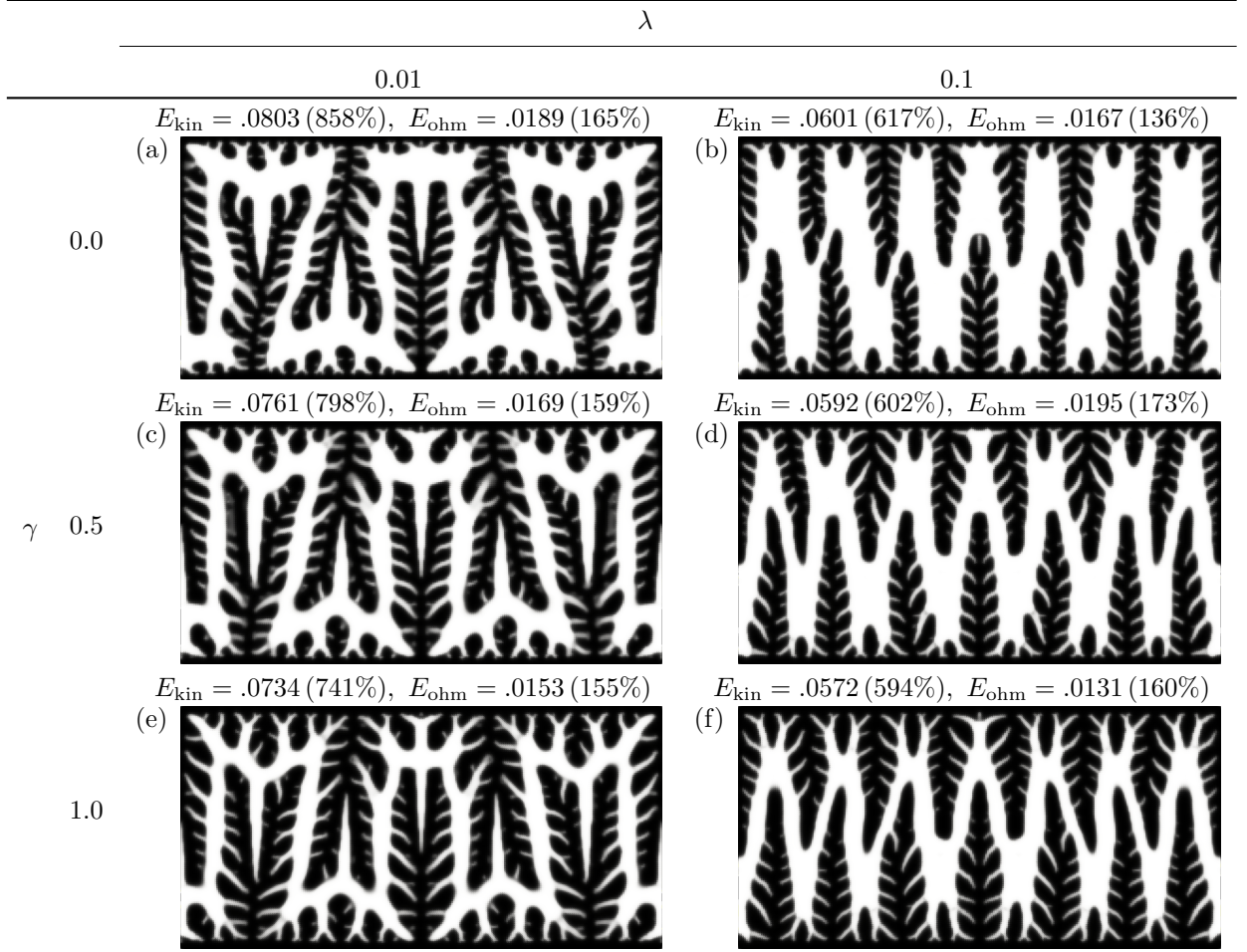
	λ	
	0.01	0.1

$E_{\mathrm{kin}} = .0803\,(858\%),\ E_{\mathrm{ohm}} = .0189\,(165\%)$ $E_{\mathrm{kin}} = .0601\,(617\%),\ E_{\mathrm{ohm}} = .0167\,(136\%)$

(a)   (b)

0.0

$E_{\mathrm{kin}} = .0761\,(798\%),\ E_{\mathrm{ohm}} = .0169\,(159\%)$ $E_{\mathrm{kin}} = .0592\,(602\%),\ E_{\mathrm{ohm}} = .0195\,(173\%)$

(c)   (d)

γ 0.5

$E_{\mathrm{kin}} = .0734\,(741\%),\ E_{\mathrm{ohm}} = .0153\,(155\%)$ $E_{\mathrm{kin}} = .0572\,(594\%),\ E_{\mathrm{ohm}} = .0131\,(160\%)$

(e)   (f)

1.0

Fig. 12: Optimized porous electrode designs modeled with the modified Bruggeman correlation, $\delta = 2$, and varying λ/γ. Black is $\bar{\rho} = 1$; white is $\bar{\rho} = 0$.

With a fixed boundary potential across all designs, a smaller cell resistance results in a stronger charging current and thus more energy storage.

E_{kin} and E_{ohm} distributions for the $\delta = 5$, $\gamma = 1$, and $\lambda = 0.01$ design with either the original or modified Bruggeman correlations are illustrated in Figs. 13 and 14. First, looking at the original Bruggeman cases in Fig. 13, notably better electrode utilization is seen in the optimized designs. Regions near the current collector in the monolithic electrodes have little energy storage, as opposed to the optimized electrodes. The optimized designs also achieve a larger energy density at the electrode tips due to their increased overpotential, which improves their material utilization by approximately 50%. The monolithic design also exhibits significant ohmic loss, in the electrode region near the separator, since the ionic currents must pass these regions to cross the gap. The ohmic loss density

in the optimized electrodes is similar, however, its net effect is less since the interdigitated structure provides more than twice as much electrode-electrolyte interface area than the monolithic design. The increased area provides additional pathways for the currents to cross the gap. Consequently, the ionic current is more uniformly distributed, resulting in less ohmic loss. This is also reflected in the 25% decrease in average cell resistance.

Analogous E_{kin} and E_{ohm} plots for designs obtained with modified Bruggeman correlation are provided in Fig. 14. We observe poor material utilization by the monolithic electrodes wherein most regions are considered "dead zones" with negligible energy storage. On the other hand, the spikey teethed optimized structures promote ion exchange, thereby the energy density is more uniformly distributed throughout the electrodes. Therefore, the overall storage is
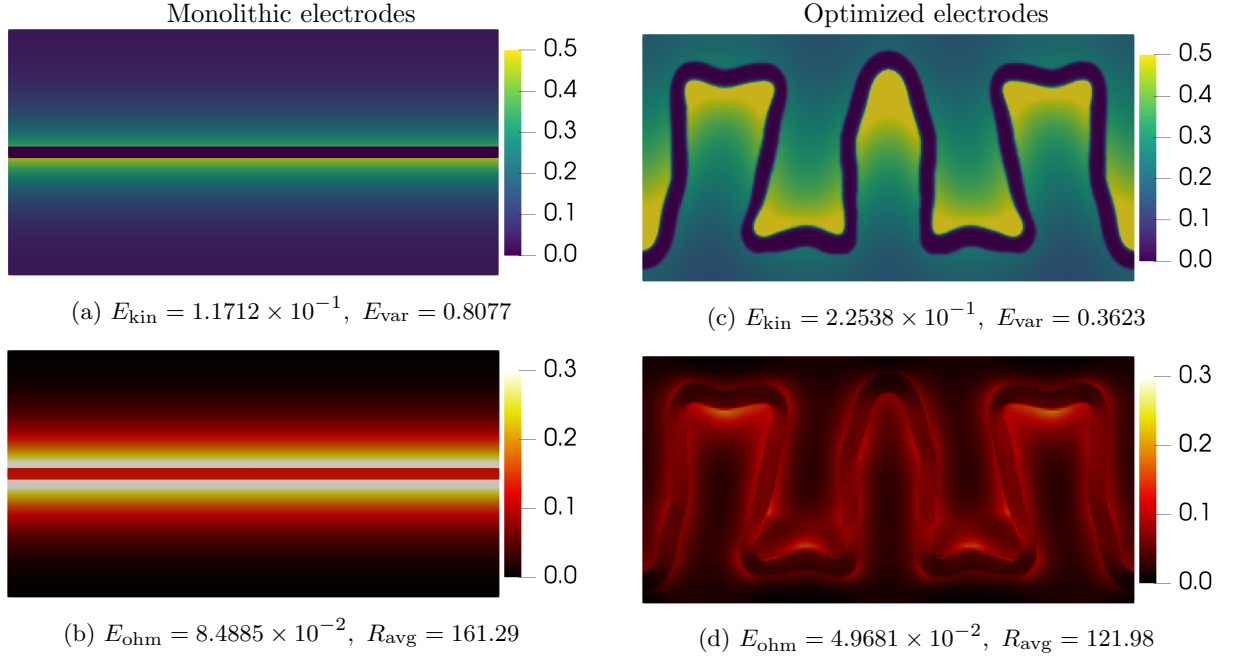
(a) $E_{\mathrm{kin}} = 1.1712 \times 10^{-1}$, $E_{\mathrm{var}} = 0.8077$

(c) $E_{\mathrm{kin}} = 2.2538 \times 10^{-1}$, $E_{\mathrm{var}} = 0.3623$

(b) $E_{\mathrm{ohm}} = 8.4885 \times 10^{-2}$, $R_{\mathrm{avg}} = 161.29$

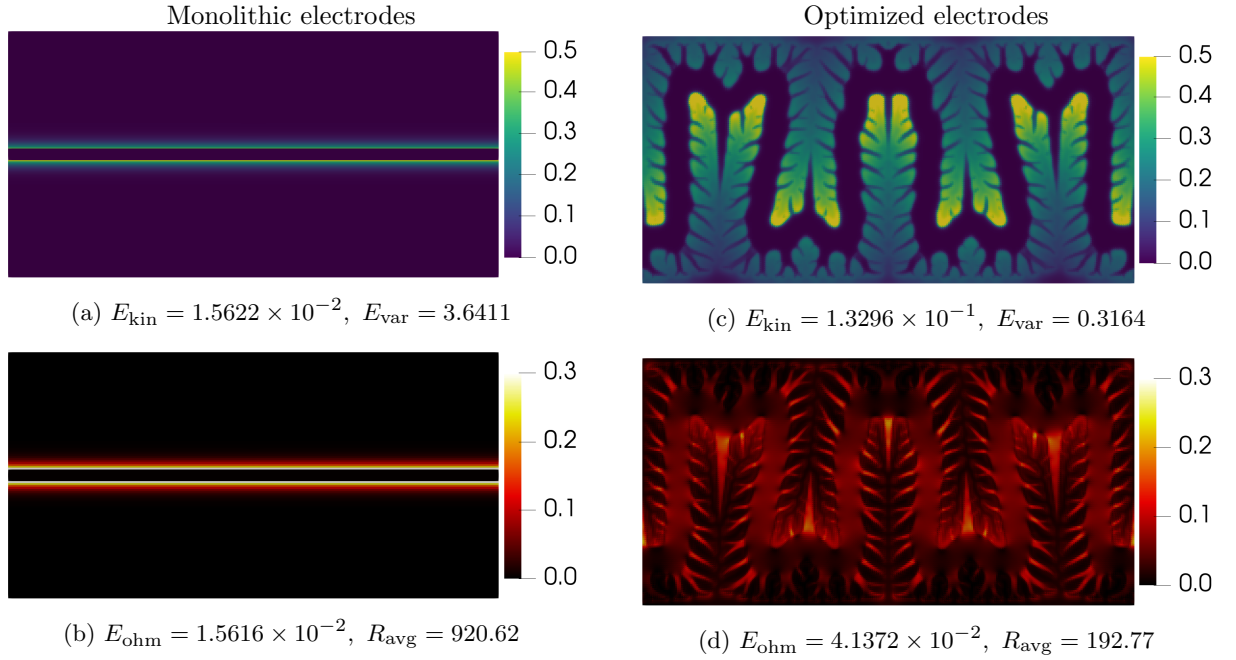(d) $E_{\mathrm{ohm}} = 4.9681 \times 10^{-2}$, $R_{\mathrm{avg}} = 121.98$

Fig. 13: Energy storage density (top) and ohmic loss density (bottom) distributions of monolithic (left) and optimized (right) electrodes with $\delta = 5$, $\gamma = 1$, $\lambda = 0.01$, and the original Bruggeman correlation.

(a) $E_{\mathrm{kin}} = 1.5622 \times 10^{-2}$, $E_{\mathrm{var}} = 3.6411$

(c) $E_{\mathrm{kin}} = 1.3296 \times 10^{-1}$, $E_{\mathrm{var}} = 0.3164$

(b) $E_{\mathrm{ohm}} = 1.5616 \times 10^{-2}$, $R_{\mathrm{avg}} = 920.62$

(d) $E_{\mathrm{ohm}} = 4.1372 \times 10^{-2}$, $R_{\mathrm{avg}} = 192.77$

Fig. 14: Energy storage density (top) and ohmic loss density (bottom) between monolithic (left) and optimized (right) electrodes with $\delta = 5$, $\gamma = 1$, $\lambda = 0.01$, and the modified Bruggeman correlation.
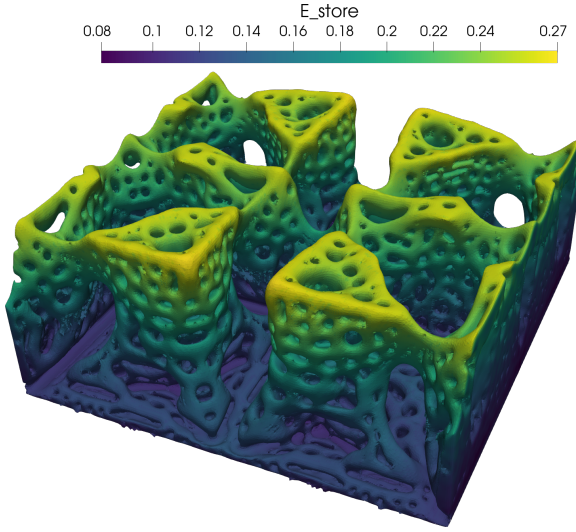
Fig. 15: Optimized anode and its energy storage distribution.

enhanced by an order of magnitude and the material utilization is enhanced by $\sim 90\%$. The ohmic loss distribution is similar to the original Bruggeman case. Although the maximum loss per unit area is significantly less for the optimized design, the total ohmic loss increases by $\sim 150\%$ due to the substantial increase in energy input. Nevertheless, we observe 5x reduction in average cell resistance. Also, the energy efficiency reaches 76%, a 26% improvement over the monolithic design.

5.4 3D example

We optimize a 3D design with $\delta = 2$, $\gamma = 0.5$, $\lambda = 0.01$, and modified Bruggeman correlation. The two optimized electrodes are similar and so we only illustrate the anode and its energy storage distribution, cf. Fig. 15. Similar protruding features of the cathode are interdigitated with these of the anode. Throughout the design of both electrodes, we observe small penetrating holes, which increase interfacial area similar to the spikey teeth from the 2D designs. From the cross sections of both electrodes plotted in Fig. 16, we observe the interdigitation similar to the 2D designs. In addition, connections between the main pillar and the wall are observed in certain locations, resulting in an arch shape. The space below the arch is filled with the arch from the other electrode, creating an interlocking structure as illustrated by the zoomed in view of Fig. 17. A simplified schematic summarizing the different design features is presented in Fig. 18
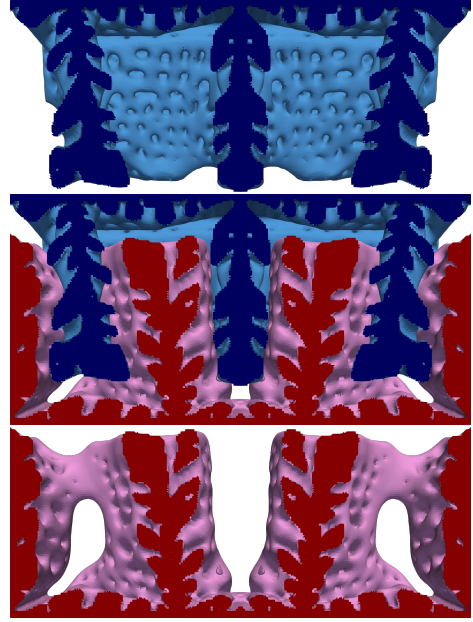

Fig. 16: Cross sections of both electrodes for 3D optimized designs. The blue (top) electrode is the cathode, and the red/pink (bottom) electrode is the anode.
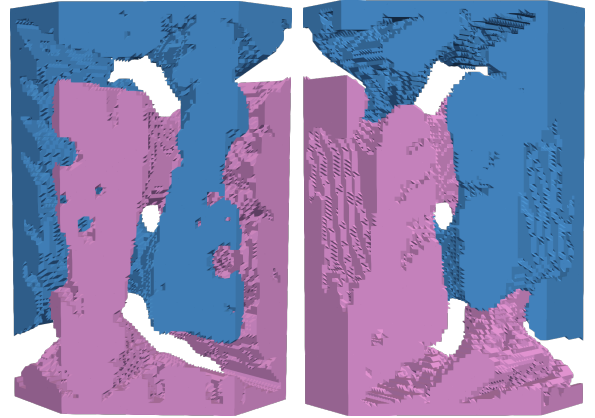

Fig. 17: Zoomed in view of the interlocking structure formed by the electrode arches.

We also compare the performance between the optimized and monolithic electrodes. The energy storage density distribution over a cross section is presented in Fig. 19 to demonstrate superior material utilization of the optimized design. Similar to the 2D observations, only the regions neighboring the separator have noticeable energy storage in the monolithic design. Better material utilization is observed in the optimized design, wherein the stored energy is more
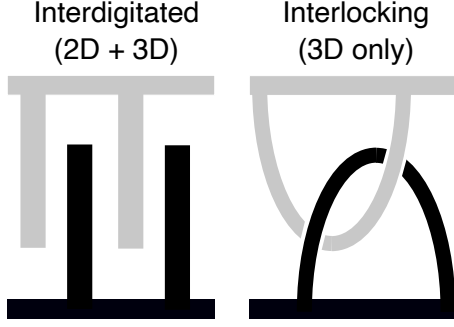
Fig. 18: Schematic of electrode structures. Both 2D and 3D cases form interdigitated columns. In addition, 3D designs also possess interlocked structure.
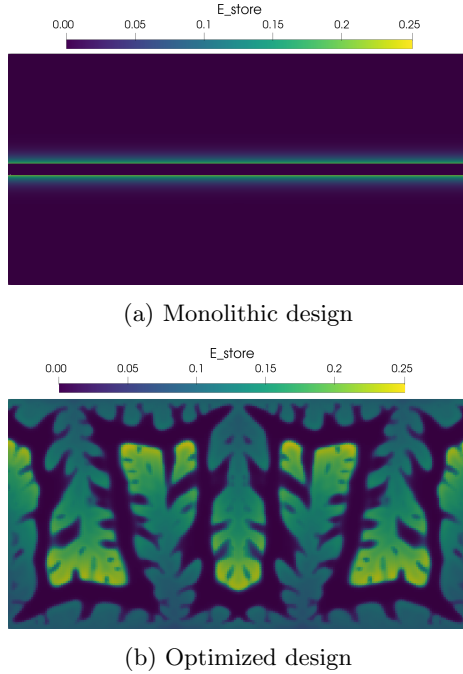

(a) Monolithic design

(b) Optimized design

Fig. 19: Cross sections of the energy storage distribution in the 3D monolithic (a) and optimized (b) designs.

uniformly distributed. The total energy storage and ohmic loss is 814% and 145% to the ones from the monolith, which is slightly better than the corresponding 2D case, possibly due to three-dimensional effects such as interlocking.

6 Conclusion

In this work, we present a density-based topology optimization strategy for the design of porous electrodes in electrochemical energy storage devices with Faradaic reactions and capacitive storage. A full-cell model is utilized to simultaneously optimize the cathode and anode.

We present various 2D optimized designs to analyze the changes in their features as we vary the value of dimensionless groups. Interdigitation is observed in all optimized designs, which unlocks additional energy storage by allowing reactions to occur closer to the opposite current collectors and by enhancing ionic transport between the electrodes. In general, more energy storage is acquired through electrode structure for $\delta = 5$ cases where reactions are localized near the separator interface. Among these cases, the designs also vary noticeably when changing between Faradaic ($\gamma = 1$) and capacitive storage-mechanisms ($\gamma = 0$). λ, i.e. the ratio between ionic and total conductivity, controls the interdigitation depth. We observe more shorter protrusions in designs with lower electronic conduction, i.e. as $\lambda \to 0.1$. Designs generated using the standard Bruggeman correlation for effective transport possess smooth surfaces. The designs generated with modified Bruggeman correlation, where effective ionic transport is much slower, possess spiky teeth cutting into the main pillars to further boost the ion exchange between the electrode and the pure electrolyte.

The key performance metrics of the optimized designs are compared against the ones from monolithic electrodes to quantify the improvements. We observe increased energy storage for all cases with the best improvement exceeding 700% from the modified Bruggeman correlation cases. Comparisons of energy storage and ohmic loss distributions suggest superior material utilization in the optimized designs. In addition, the ohmic loss is more evenly distributed and thus does not grow significantly even when the total charging current increases by an order of magnitude.

Finally, a 3D design is generated to further demonstrate the utility of the proposed optimization strategy. More complex features, such as channels, holes, and interlocking arches between the electrodes are observed in this design.

As mentioned above, our current work does not track surface or solid concentrations. To address this, our future work may incorporate diffusion in the solid particles as in the Doyle-Fuller-Newman model (Doyle et al, 1993). Typically used for a 1D geometry, this model includes diffusion inside spherical particles, making it a pseudo-2D model. For 3D geometries, this

becomes a pseudo-4D model, further exacerbating the computational effort.

Funding information

A Energy balance derivation

We derive the energy balance for the dimensionless system with energy input, energy storage, and ohmic loss. We first scale the electric and ionic potential equation such that the source terms are the same:

$$-\frac{1}{\lambda}\hat{\nabla}\cdot\left(\hat{\sigma}\hat{\nabla}\hat{\Phi}_1\right) = -\delta_r\hat{a}\hat{i}_n - \delta_c\hat{a}\hat{i}_c,$$

$$-\frac{1}{1-\lambda}\hat{\nabla}\cdot(\hat{D}\hat{c}\hat{\nabla}\hat{\Phi}_2) - \frac{1}{1-\lambda}\left(\frac{t_{0,+}}{z_+} + \frac{t_{0,-}}{z_-}\right) \quad (42)$$

$$\hat{\nabla}\cdot(\hat{D}\hat{\nabla}\hat{c}) = \delta_r\hat{a}\hat{i}_n + \delta_c\hat{a}\hat{i}_c.$$

Since $\hat{\Phi}_1 = 0$ on $\hat{\Gamma}_a$ and $\nabla\hat{\Phi}_1\cdot\mathbf{n} = 0$ on $\partial\hat{\Omega}\setminus(\hat{\Gamma}_a\bigcup\hat{\Gamma}_c)$ the dimensionless energy input can be expressed as

$$E_{\text{in}} = \frac{1}{\lambda}\int_0^{\hat{T}}\int_{\hat{\Gamma}_c}\hat{\sigma}\hat{\nabla}\hat{\Phi}_1\cdot\mathbf{n}\hat{\Phi}_1\,\mathrm{d}\hat{s}\,\mathrm{d}\hat{t}$$

$$= \frac{1}{\lambda}\int_0^{\hat{T}}\int_{\partial\hat{\Omega}}\hat{\sigma}\hat{\nabla}\hat{\Phi}_1\cdot\mathbf{n}\hat{\Phi}_1\,\mathrm{d}\hat{s}\,\mathrm{d}\hat{t}, \quad (43)$$

which extends integral from the cathode current collector $\hat{\Gamma}_c$ to the entire boundary $\partial\hat{\Omega}$. With $\hat{\nabla}\hat{\Phi}_2\cdot\mathbf{n} = 0$ and $\hat{\nabla}\hat{c}\cdot\mathbf{n} = 0$ on $\partial\hat{\Omega}$, the dimensionless energy input can be further extended as

$$E_{\text{in}} = \frac{1}{\lambda}\int_0^{\hat{T}}\int_{\partial\hat{\Omega}}\hat{\sigma}\hat{\nabla}\hat{\Phi}_1\cdot\mathbf{n}\hat{\Phi}_1\,\mathrm{d}\hat{s}\,\mathrm{d}\hat{t}$$

$$+ \frac{1}{1-\lambda}\int_0^{\hat{T}}\int_{\partial\hat{\Omega}}\hat{D}\hat{c}\hat{\nabla}\hat{\Phi}_2\cdot\mathbf{n}\hat{\Phi}_2\,\mathrm{d}\hat{s}\,\mathrm{d}\hat{t}$$

$$+ \frac{1}{1-\lambda}\left(\frac{t_{0,+}}{z_+} + \frac{t_{0,-}}{z_-}\right)\int_0^{\hat{T}}\int_{\partial\hat{\Omega}}\hat{D}\hat{\nabla}\hat{c}\cdot\mathbf{n}\hat{\Phi}_2\,\mathrm{d}\hat{s}\,\mathrm{d}\hat{t}, \quad (44)$$

Applying the divergence theorem we obtain

$$E_{\text{in}} = \frac{1}{\lambda}\int_0^{\hat{T}}\int_{\hat{\Omega}}\hat{\nabla}\cdot\left(\hat{\sigma}\hat{\nabla}\hat{\Phi}_1\hat{\Phi}_1\right)\,\mathrm{d}\hat{x}\,\mathrm{d}\hat{t}$$

$$+ \frac{1}{1-\lambda}\int_0^{\hat{T}}\int_{\hat{\Omega}}\hat{\nabla}\cdot\left(\hat{D}\hat{c}\hat{\nabla}\hat{\Phi}_2\hat{\Phi}_2\right)\,\mathrm{d}\hat{x}\,\mathrm{d}\hat{t}$$

$$+ \frac{1}{1-\lambda}\left(\frac{t_{0,+}}{z_+} + \frac{t_{0,-}}{z_-}\right)\int_0^{\hat{T}}\int_{\hat{\Omega}}\hat{\nabla}\cdot\left(\hat{D}\hat{\nabla}\hat{c}\hat{\Phi}_2\right)\,\mathrm{d}\hat{x}\,\mathrm{d}\hat{t}. \quad (45)$$

An application of the product rule subsequently gives

$$E_{\text{in}} = \frac{1}{\lambda}\int_0^{\hat{T}}\int_{\hat{\Omega}}\hat{\sigma}\hat{\nabla}\hat{\Phi}_1\cdot\hat{\nabla}\hat{\Phi}_1\,\mathrm{d}\hat{x}\,\mathrm{d}\hat{t}$$

$$+ \frac{1}{\lambda}\int_0^{\hat{T}}\int_{\hat{\Omega}}\hat{\nabla}\cdot(\hat{\sigma}\hat{\nabla}\hat{\Phi}_1)\hat{\Phi}_1\,\mathrm{d}\hat{x}\,\mathrm{d}\hat{t}$$

$$+ \frac{1}{1-\lambda}\int_0^{\hat{T}}\int_{\hat{\Omega}}\hat{D}\hat{c}\hat{\nabla}\hat{\Phi}_2\cdot\hat{\nabla}\hat{\Phi}_2\,\mathrm{d}\hat{x}\,\mathrm{d}\hat{t}$$

$$+ \frac{1}{1-\lambda}\int_0^{\hat{T}}\int_{\hat{\Omega}}\hat{\nabla}\cdot(\hat{D}\hat{c}\hat{\nabla}\hat{\Phi}_2)\hat{\Phi}_2\,\mathrm{d}\hat{x}\,\mathrm{d}\hat{t}$$

$$+ \frac{1}{1-\lambda}\left(\frac{t_{0,+}}{z_+} + \frac{t_{0,-}}{z_-}\right)\int_0^{\hat{T}}\int_{\hat{\Omega}}\hat{D}\hat{\nabla}\hat{c}\cdot\hat{\nabla}\hat{\Phi}_2\,\mathrm{d}\hat{x}\,\mathrm{d}\hat{t}$$

$$+ \frac{1}{1-\lambda}\left(\frac{t_{0,+}}{z_+} + \frac{t_{0,-}}{z_-}\right)\int_0^{\hat{T}}\int_{\hat{\Omega}}\hat{\nabla}\cdot(\hat{D}\hat{\nabla}\hat{c})\hat{\Phi}_2\,\mathrm{d}\hat{x}\,\mathrm{d}\hat{t}. \quad (46)$$

Combining (42) and (46) yields

$$E_{\text{in}} = \frac{1}{\lambda}\int_0^{\hat{T}}\int_{\hat{\Omega}}\hat{\sigma}\hat{\nabla}\hat{\Phi}_1\cdot\hat{\nabla}\hat{\Phi}_1\,\mathrm{d}\hat{x}\,\mathrm{d}\hat{t}$$

$$+ \frac{1}{1-\lambda}\int_0^{\hat{T}}\int_{\hat{\Omega}}\hat{D}\hat{c}\hat{\nabla}\hat{\Phi}_2\cdot\hat{\nabla}\hat{\Phi}_2\,\mathrm{d}\hat{x}\,\mathrm{d}\hat{t}$$

$$+ \frac{1}{1-\lambda}\left(\frac{t_+}{z_+} + \frac{t_-}{z_-}\right)\int_0^{\hat{T}}\int_{\hat{\Omega}}\hat{D}\hat{\nabla}\hat{c}\cdot\hat{\nabla}\hat{\Phi}_2\,\mathrm{d}\hat{x}\,\mathrm{d}\hat{t} \quad (47)$$

$$+ \delta_r\int_0^{\hat{T}}\int_{\hat{\Omega}}\hat{a}\hat{i}_n(\hat{\Phi}_1 - \hat{\Phi}_2)\,\mathrm{d}\hat{x}\,\mathrm{d}\hat{t}$$

$$+ \delta_c\int_0^{\hat{T}}\int_{\hat{\Omega}}\hat{a}\hat{i}_c(\hat{\Phi}_1 - \hat{\Phi}_2)\,\mathrm{d}\hat{x}\,\mathrm{d}\hat{t},$$

which is equivalent to $E_{\text{in}} = E_{\text{kin}} + E_{\text{ohm}}$.

B Mixed discretizations

A mixed formulation is utilized to solve the filter problem (2) to obtain piecewise constant $\tilde{\rho}$ over triangular and tetrahedral meshes. In this way, we are sure that $\tilde{\rho}(\mathbf{x}) \in [0, 1]$. Indeed, the mixed method enforces flux continuity across the element interfaces, which prevents oscillations in the filtered field as the control field goes to $\{0, 1\}$ (Salazar de Troya and Tortorelli, 2020). As opposed to the two-point flux approximation scheme from Roy et al (2022), no orthogonality condition is required on the mesh regularity.

With $r^2 > 0$, we define the auxiliary flux term as

$$r^{-2}\boldsymbol{u}_f = -\nabla\tilde{\rho}. \quad (48)$$

Then the filter problem is rewritten as

$$\begin{aligned} r^{-2}\boldsymbol{u}_f + \nabla\tilde{\rho} &= 0 &&\text{in } \Omega, \\ -\nabla\cdot\boldsymbol{u}_f - \tilde{\rho} &= -\rho &&\text{in } \Omega, \\ \boldsymbol{u}_f\cdot\mathbf{n} &= 0 &&\text{on } \partial\Omega. \end{aligned} \quad (49)$$

The function spaces for the mixed weak variational form are

$$\boldsymbol{V} = \{\boldsymbol{v} \in H(\mathrm{div}, \Omega) \mid \boldsymbol{v} \cdot \mathbf{n} = 0 \text{ on } \partial\Omega\}, \ \ W = L^2(\Omega), \tag{50}$$

where the Neumann flux boundary condition are imposed strongly. We seek to find $(\boldsymbol{u}_f, \tilde{\rho}) \in \boldsymbol{V} \times W$ such that

$$\begin{aligned}(r^{-2}\boldsymbol{u}_f, \boldsymbol{v})_\Omega - (\tilde{\rho}, \nabla \cdot \boldsymbol{v})_\Omega &= 0, \\ -(\nabla \cdot \boldsymbol{u}_f, w)_\Omega - (\tilde{\rho}, w)_\Omega &= -(\rho, w)_\Omega,\end{aligned} \tag{51}$$

$\forall (\boldsymbol{v}, w) \in \boldsymbol{V} \times W$.

A similar mixed formulation is used for solving the boundary propagation PDE (4). From (4), since $\bar{\rho}$ is strictly positive, we define the auxiliary flux term as

$$\bar{\rho}^{-1}\boldsymbol{u}_b = -\nabla\beta. \tag{52}$$

Then the continuous boundary propagation problem can be reformulated as

$$\begin{aligned}\bar{\rho}^{-1}\boldsymbol{u}_b + \nabla\beta &= 0 & &\text{in } \Omega, \\ -\nabla \cdot \boldsymbol{u}_b - (1 - \bar{\rho})\beta &= 0 & &\text{in } \Omega, \\ \beta &= 1 & &\text{on } \Gamma_\mathrm{a}, \\ \beta &= -1 & &\text{on } \Gamma_\mathrm{c}, \\ \boldsymbol{u}_b \cdot \mathbf{n} &= 0 & &\text{on } \partial\Omega/\Gamma_\mathrm{c} \cup \Gamma_\mathrm{a}.\end{aligned} \tag{53}$$

Let $\Gamma_D = \Gamma_a \cup \Gamma_c$. We introduce the function space

$$\boldsymbol{V}_D = \{\boldsymbol{v} \in H(\mathrm{div}, \Omega) | \boldsymbol{v} \cdot \mathbf{n} = 0 \text{ on } \Gamma_D\}. \tag{54}$$

We seek to find $(\boldsymbol{u}_b, \beta) \in \boldsymbol{V}_D \times W$ such that

$$\begin{aligned}(\bar{\rho}^{-1}\boldsymbol{u}_b, \boldsymbol{v})_\Omega - (\beta, \nabla \cdot \boldsymbol{v})_\Omega &= \\ -\langle 1, \boldsymbol{v} \cdot \mathbf{n}\rangle_{\Gamma_\mathrm{a}} &- \langle -1, \boldsymbol{v} \cdot \mathbf{n}\rangle_{\Gamma_\mathrm{c}}, \\ -(\nabla \cdot \boldsymbol{u}_b, w)_\Omega - ((1 - \bar{\rho})\beta, w)_\Omega &= 0,\end{aligned} \tag{55}$$

$\forall (\boldsymbol{v}, w) \in \boldsymbol{V}_D \times W$. Both problems use Raviart-Thomas basis functions with the lowest order to obtain the discretized solution, which results in piecewise constant $\tilde{\rho}/\beta$ and piecewise linear $\boldsymbol{u}_f/\boldsymbol{u}_b$ with continuous normal flux across the element interfaces.

For the three-dimensional case, we use an iterative method to solve the linear systems resulting from the weak forms described by (51) and (55). These systems have symmetric block matrices of the form

$$\begin{bmatrix} A & B \\ B^\top & D \end{bmatrix} \tag{56}$$

where A represents a weighted mass matrix for the flux, D is a weighted mass matrix for $\tilde{\rho}$ or β, and B is the coupling term. The approach introduced in Silvester and Wathen (1994) is used to solve the block system efficiently. The block matrix (56) admits a factorization of the type

$$\begin{bmatrix} A & B \\ B^\top & D \end{bmatrix} = \begin{bmatrix} I & 0 \\ B^\top A^{-1} & I \end{bmatrix} \begin{bmatrix} A & 0 \\ 0 & S \end{bmatrix} \begin{bmatrix} I & A^{-1}B \\ 0 & I \end{bmatrix}, \tag{57}$$

where $S = D - CA^{-1}B$ is called the *Schur complement.* The inverse of the block matrix is

$$\begin{bmatrix} A & B \\ B^\top & D \end{bmatrix}^{-1}$$
$$= \begin{bmatrix} I & -A^{-1}B \\ 0 & I \end{bmatrix} \begin{bmatrix} A^{-1} & 0 \\ 0 & S^{-1} \end{bmatrix} \begin{bmatrix} I & 0 \\ -B^\top A^{-1} & I \end{bmatrix}, \tag{58}$$

which requires inverting the blocks A and S. Our preconditioner approximates the blocks of this factorization. We approximate the Schur complements using the diagonal of A, i.e. we use the sparse $\tilde{S} = D - C\mathrm{diag}(A)^{-1}B$. The inverse of $\tilde{S}$ is approximated by Algebraic Multigrid (Ruge and Stüben, 1987), and the inverse of A is approximated by a block incomplete LU factorization with 0 fill (ILU0) (Meijerink and Van Der Vorst, 1977). The PETSc solver options used for the three-dimensional simulations are given in Appendix C.

C PETSc solver options

Here we provide he PETSc solver options used for the three-dimensional case. The options for solving the governing physical system are:

```
 1    "snes_rtol": 0,
 2    "snes_atol": 1e-4,
 3    "mat_type": "aij",
 4    "ksp_type": "gmres",
 5    "ksp_rtol": 1e-4,
 6    "ksp_gmres_restart": 30,
 7    "pc_type": "fieldsplit",
 8    "pc_fieldsplit_type": "multiplicative",
 9    "fieldsplit_pc_type": "hypre",
10    "fieldsplit_pc_hypre_boomeramg": {
11        "strong_threshold": 0.7,
12        "coarsen_type": "HMIS",
13        "agg_nl": 3,
14        "interp_type": "ext+i",
15        "agg_num_paths": 5,
16        },
```

The options for the mixed formulation used for the filtering and boundary propagation problems are:

```
 1    "mat_type": "nest",
 2    "ksp_type": "gmres",
 3    "ksp_rtol": 1e-4,
 4    "pc_type": "fieldsplit",
 5    "pc_fieldsplit_type": "schur",
 6    "pc_fieldsplit_schur_fact_type": "full",
 7    "fieldsplit_0_ksp_type": "preonly",
 8    "fieldsplit_0_pc_type": "bjacobi",
 9    "fieldsplit_0_sub_pc_type": "ilu",
10    "fieldsplit_1_ksp_type": "preonly",
11    "pc_fieldsplit_schur_precondition": "selfp",
12    "fieldsplit_1_pc_type": "hypre",
13    "fieldsplit_1_pc_hypre_boomeramg": {
14        "strong_threshold": 0.7,
15        "coarsen_type": "HMIS",
16        "agg_nl": 3,
17        "interp_type": "ext+i",
18        "agg_num_paths": 5,
19        }.
```

References

Alizadeh M, Charoen-amornkitt P, Suzuki T, et al (2023) A numerical simulation of evolution processes and entropy generation for optimal architecture of an electrochemical reaction-diffusion system: Comparison of two optimization strategies. Journal of The Electrochemical Society https://doi.org/10.1149/1945-7111/ad0a7c, URL http://iopscience.iop.org/article/10.1149/1945-7111/ad0a7c

Balay S, Abhyankar S, Adams MF, et al (2023a) PETSc/TAO users manual. Tech. Rep. ANL-21/39 - Revision 3.20, Argonne National Laboratory, https://doi.org/10.2172/1968587

Balay S, Abhyankar S, Adams MF, et al (2023b) PETSc Web page. https://petsc.org/, URL https://petsc.org/

Batista MDR, Chandrasekaran S, Moran BD, et al (2023) Design and additive manufacturing of optimized electrodes for energy storage applications. Carbon 205:262–269. https://doi.org/10.1016/j.carbon.2023.01.044

Beck VA, Ivanovskaya AN, Chandrasekaran S, et al (2021a) Inertially enhanced mass transport using 3D-printed porous flow-through electrodes with periodic lattice structures. Proceedings of the National Academy of Sciences 118(32):e2025562,118. https://doi.org/10.1073/pnas.2025562118

Beck VA, Wong JJ, Jekel CF, et al (2021b) Computational design of microarchitected porous electrodes for redox flow batteries. Journal of Power Sources 512:230,453. https://doi.org/10.1016/j.jpowsour.2021.230453

Behrou R, Pizzolato A, Forner-Cuenca A (2019) Topology optimization as a powerful tool to design advanced PEMFCs flow fields. International Journal of Heat and Mass Transfer 135:72–92. https://doi.org/10.1016/j.ijheatmasstransfer.2019.01.050

Bendsøe MP (1989) Optimal shape design as a material distribution problem. Structural optimization 1(4):193–202. https://doi.org/10.1007/bf01650949

Bourdin B (2001) Filters in topology optimization. International Journal for Numerical Methods in Engineering 50(9):2143–2158

Brandt A (1977) Multi-level adaptive solutions to boundary-value problems. Mathematics of Computation 31(138):333–390. https://doi.org/10.1090/s0025-5718-1977-0431719-x

Brosa Planella F, Ai W, Boyce AM, et al (2022) A continuum of physics-based lithium-ion battery models reviewed. Progress in Energy 4(4):042,003. https://doi.org/10.1088/2516-1083/ac7d31

Bruggeman VD (1935) Berechnung verschiedener physikalischer konstanten von heterogenen substanzen. i. dielektrizitätskonstanten und leitfähigkeiten der mischkörper aus isotropen substanzen. Annalen der physik 416(7):636–664. https://doi.org/10.1002/andp.19374210205

Bruns TE, Tortorelli DA (2001) Topology optimization of non-linear elastic structures and compliant mechanisms. Computer Methods in Applied Mechanics and Engineering 190(26-27):3443–3459

Chandrasekaran S, Lin D, Li Y, et al (2023) Aerogels, additive manufacturing, and energy storage. Joule 7(5):866–883

Chen CH, Yaji K, Yamasaki S, et al (2019) Computational design of flow fields for vanadium redox flow batteries via topology optimization. Journal of Energy Storage 26:100,990. https://doi.org/10.1016/j.est.2019.100990

Chen KH, Namkoong MJ, Goel V, et al (2020) Efficient fast-charging of lithium-ion batteries enabled by laser-patterned three-dimensional graphite anode architectures. Journal of Power Sources 471:228,475

Chu S, Majumdar A (2012) Opportunities and challenges for a sustainable energy future. Nature 488(7411):294–303. https://doi.org/10.1038/nature11475

Chu S, Cui Y, Liu N (2016) The path towards sustainable energy. Nature Materials 16(1):16–22. https://doi.org/10.1038/nmat4834

Chu T, Park S, Fu KK (2021) 3D printing-enabled advanced electrode architecture design. Carbon Energy 3(3):424–439

Doyle M, Fuller TF, Newman J (1993) Modeling of galvanostatic charge and discharge of the lithium/polymer/insertion cell. Journal of The Electrochemical Society 140(6):1526. https://doi.org/10.1149/1.2221597

Falgout RD, Yang UM (2002) hypre: A library of high performance preconditioners. In: International Conference on Computational Science, Springer, pp 632–641, https://doi.org/10.1007/3-540-47789-6_66

Fuller TF, Harb JN (2018) Electrochemical Engineering. John Wiley & Sons, Hoboken, NJ USA

Gallagher KG, Trask SE, Bauer C, et al (2015) Optimizing areal capacities through understanding the limitations of lithium-ion electrodes. Journal of The Electrochemical Society 163(2):A138

Gao Y, Cao Q, Pu J, et al (2023) Stable Zn anodes with triple gradients. Advanced Materials 35(6):2207,573

Golmon S, Maute K, Dunn ML (2012) Multiscale design optimization of lithium ion batteries using adjoint sensitivity analysis. International Journal for Numerical Methods in Engineering 92(5):475–494. https://doi.org/10.1002/nme.4347

Griewank A, Walther A (2000) Algorithm 799: Revolve: An implementation of checkpointing for the reverse or adjoint mode of computational differentiation. ACM Trans Math Softw 26(1):19–45. https://doi.org/10.1145/347837.347846

Guest JK, Prévost JH, Belytschko T (2004) Achieving minimum length scale in topology optimization using nodal design variables and projection functions. International journal for numerical methods in engineering 61(2):238–254. https://doi.org/10.1002/nme.1064

Gür TM (2018) Review of electrical energy storage technologies, materials and systems: challenges and prospects for large-scale grid storage. Energy & Environmental Science 11(10):2696–2767. https://doi.org/10.1039/c8ee01419a

Ham DA, Kelly PHJ, Mitchell L, et al (2023) Firedrake User Manual. Imperial College London and University of Oxford and Baylor University and University of Washington, first edition edn., https://doi.org/10.25561/104839

Hart RW, White HS, Dunn B, et al (2003) 3-D microbatteries. Electrochemistry Communications 5(2):120–123

Henson VE, Yang UM (2002) BoomerAMG: A parallel algebraic multigrid solver and preconditioner. Applied Numerical Mathematics 41(1):155–177. https://doi.org/10.1016/s0168-9274(01)00115-5

Heubner C, Voigt K, Marcinkowski P, et al (2021) From active materials to battery cells: A straightforward tool to determine performance metrics and support developments at an application-relevant level. Advanced Energy Materials 11(46):2102,647

Hung CH, Allu S, Cobb CL (2021) Modeling current density non-uniformities to understand high-rate limitations in 3D interdigitated lithium-ion batteries. Journal of the Electrochemical Society 168(10):100,512

Hung CH, Huynh P, Teo K, et al (2022) Are three-dimensional batteries beneficial? analyzing historical data to elucidate performance advantages. ACS Energy Letters 8(1):296–305

Johnson A, Newman J (1971) Desalting by means of porous carbon electrodes. Journal of The Electrochemical Society 118(3):150. https://doi.org/10.1149/1.2408094

Kuang Y, Chen C, Kirsch D, et al (2019) Thick electrode batteries: Principles, opportunities, and challenges. Advanced Energy Materials 9(33):1901,457. https://doi.org/https:

//doi.org/10.1002/aenm.201901457, URL https://onlinelibrary.wiley.com/doi/abs/10.1002/aenm.201901457

Lazarov BS, Sigmund O (2011) Filters in topology optimization based on Helmholtz-type differential equations. International Journal for Numerical Methods in Engineering 86(6):765–781. https://doi.org/10.1002/nme.3072

Lazarov BS, Wang F, Sigmund O (2016) Length scale and manufacturability in density-based topology optimization. Archive of Applied Mechanics 86:189–218. https://doi.org/10.1007/s00419-015-1106-4

Lin TY, Baker SE, Duoss EB, et al (2022) Topology optimization of 3D flow fields for flow batteries. Journal of The Electrochemical Society 169(5):050,540. https://doi.org/10.1149/1945-7111/ac716d

Long JW, Dunn B, Rolison DR, et al (2004) Three-dimensional battery architectures. Chemical Reviews 104(10):4463–4492

Long JW, Dunn B, Rolison DR, et al (2020) 3D architectures for batteries and electrodes. Advanced Energy Materials 10(46):2002,457

Lyu Z, Lim G, Koh JJ, et al (2021) Design and manufacture of 3D-printed batteries. Joule 5:89–114

Madabattula G, Kumar S (2020) Model and measurement based insights into double layer capacitors: Voltage-dependent capacitance and low ionic conductivity in pores. Journal of The Electrochemical Society 167(8):080,535. https://doi.org/10.1149/1945-7111/ab90aa

Meijerink JA, Van Der Vorst HA (1977) An iterative solution method for linear systems of which the coefficient matrix is a symmetric M-matrix. Mathematics of computation 31(137):148–162. https://doi.org/10.2307/2005786

Mitusch SK, Funke SW, Dokken JS (2019) dolfin-adjoint 2018.1: automated adjoints for FEniCS and Firedrake. Journal of Open Source Software 4(38):1292. https://doi.org/10.21105/joss.01292

Newman J, Thomas-Alyea KE (2012) Electrochemical systems. John Wiley & Sons

Newman J, Tiedemann W (1975) Porous-electrode theory with battery applications. AlChE Journal 21(1):25–41. https://doi.org/10.1002/aic.690210103

Newman JS, Tobias CW (1962) Theoretical analysis of current distribution in porous electrodes. Journal of The Electrochemical Society 109(12):1183. https://doi.org/10.1149/1.2425269

Qu C, Zhang Y, Zhang Z, et al (2023) Design of radial flow channel proton exchange membrane fuel cell based on topology optimization. Processes 11(8):2482. https://doi.org/10.3390/pr11082482

Ramadesigan V, Methekar RN, Latinwo F, et al (2010) Optimal porosity distribution for minimized ohmic drop across a porous electrode. Journal of The Electrochemical Society 157(12):A1328. https://doi.org/10.1149/1.3495992

Roy T, Salazar de Troya MA, Worsley MA, et al (2022) Topology optimization for the design of porous electrodes. Structural and Multidisciplinary Optimization 65(171). https://doi.org/10.1007/s00158-022-03249-2

Ruge JW, Stüben K (1987) Algebraic multigrid. In: Multigrid methods, vol 3 of Frontiers in Applied Mathematics. SIAM, Philadelphia, chap 4, p 73–130, https://doi.org/10.1137/1.9781611971057.ch4

Sá LF, Okubo Jr. CM, Sá AN, et al (2022) Continuous boundary condition propagation model for topology optimization. Structural and Multidisciplinary Optimization 65(15). https://doi.org/10.1007/s00158-021-03148-y

Saad Y, Schultz MH (1986) Gmres: A generalized minimal residual algorithm for solving nonsymmetric linear systems. SIAM Journal on scientific and statistical computing 7(3):856–869. https://doi.org/10.1137/0907058

Sigmund O (2007) Morphology-based black and white filters for topology optimization. Structural and Multidisciplinary Optimization 33:401–424. https://doi.org/10.1007/s00158-006-0087-x

Sigmund O, Maute K (2013) Topology optimization approaches: A comparative review. Structural and multidisciplinary optimization 48(6):1031–1055. https://doi.org/10.1007/s00158-013-0978-6

Sigmund O, Torquato S (1997) Design of materials with extreme thermal expansion using a three-phase topology optimization method. Journal of the Mechanics and Physics of Solids 45(6):1037–1067. https://doi.org/10.1016/S0022-5096(96)00114-7

Silvester D, Wathen A (1994) Fast iterative solution of stabilised stokes systems part II: Using general block preconditioners. SIAM Journal on Numerical Analysis 31(5):1352–1367. https://doi.org/10.1137/0731070

Simon P, Gogotsi Y, Dunn B (2014) Where do batteries end and supercapacitors begin? Science 343(6176):1210–1211

Singh M, Kaiser J, Hahn H (2015) Thick electrodes for high energy lithium ion batteries. Journal of The Electrochemical Society 162(7):A1196

Soares DM, Ren Z, Mujib SB, et al (2021) Additive manufacturing of electrochemical energy storage systems electrodes. Advanced Energy and Sustainability Research 2(5):2000,111

Svanberg K (1987) The method of moving asymptotes – a new method for structural optimization. International journal for numerical methods in engineering 24(2):359–373. https://doi.org/10.1002/nme.1620240207

Tjaden B, Cooper SJ, Brett DJ, et al (2016) On the origin and application of the Bruggeman correlation for analysing transport phenomena in electrochemical systems. Current Opinion in Chemical Engineering 12:44–51. https://doi.org/10.1016/j.coche.2016.02.006

Tjaden B, Brett DJ, Shearing PR (2018) Tortuosity in electrochemical devices: a review of calculation approaches. International Materials Reviews 63(2):47–67. https://doi.org/10.1080/09506608.2016.1249995

Trembacki B, Duoss E, Oxberry G, et al (2019) Mesoscale electrochemical performance simulation of 3D interpenetrating lithium-ion battery electrodes. Journal of The Electrochemical Society 166(6):A923—A934

Salazar de Troya MA (2021) LLNL/pyMMAopt: Method of Moving Asymptotes for Firedrake. https://doi.org/10.5281/zenodo.5524961

Salazar de Troya MA, Tortorelli DA (2020) Three-dimensional adaptive mesh refinement in stress-constrained topology optimization. Structural and Multidisciplinary Optimization 62(5):2467–2479. https://doi.org/10.1007/s00158-020-02618-z

Wang DW, Li F, Liu M, et al (2008) 3D aperiodic hierarchical porous graphitic carbon material for high-rate electrochemical capacitive energy storage. Angewandte Chemie International Edition 47(2):373–376. https://doi.org/10.1002/ange.200702721

Wang Y, Chen C, Xie H, et al (2017) 3D-printed all-fiber Li-ion battery toward wearable energy storage. Advanced Functional Materials 27(43):1703,140

Wang Z, Wang H, Xiao H, et al (2023) Enhancing heat dissipation and mass transfer of oxygen gas flow channel in a proton exchange membrane fuel cell using multiobjective topology optimization. International Journal of Hydrogen Energy 48(83):32,495–32,511. https://doi.org/https://doi.org/10.1016/j.ijhydene.2023.05.023

Wathen AJ (2015) Preconditioning. Acta Numerica 24:329–376. https://doi.org/10.1017/s0962492915000021

Watts S, Tortorelli DA (2016) An n-material thresholding method for improving integerness of solutions in topology optimization. International Journal for Numerical Methods in Engineering 108(12):1498–1524. https://doi.org/10.

1002/nme.5265

Xu M, Reichman B, Wang X (2019) Modeling the effect of electrode thickness on the performance of lithium-ion batteries with experimental validation. Energy 186:115,864. https://doi.org/ https://doi.org/10.1016/j.energy.2019.115864, URL https://www.sciencedirect.com/science/ article/pii/S0360544219315361

Xu S, Cai Y, Cheng G (2010) Volume preserving nonlinear density filter based on heaviside functions. Structural and Multidisciplinary Optimization 41:495–505. https://doi.org/10.1007/ s00158-009-0452-7

Xue N, Du W, Martins JR, et al (2015) Lithiumion batteries: Thermomechanics, performance, and design optimization. In: Handbook of Clean Energy Systems, John Wiley & Sons Ltd., vol. 6. Wiley Online Library, p 2849–2864, https: //doi.org/10.1002/9781118991978.hces225

Yaji K, Yamasaki S, Tsushima S, et al (2018) Topology optimization for the design of flow fields in a redox flow battery. Structural and multidisciplinary optimization 57(2):535–546. https://doi.org/10.1007/s00158-017-1763-8

Yang J, Li Y, Mijailovic A, et al (2022) Gradient porosity electrodes for fast charging lithiumion batteries. Journal of Materials Chemistry A 10(22):12,114–12,124

Zadin V, Brandell D, Kasemägi H, et al (2011) Finite element modelling of ion transport in the electrolyte of a 3D-microbattery. Solid State Ionics 192(1):279–283

Zekoll S, Marriner-Edwards C, Hekselman AKO, et al (2018) Hybrid electrolytes with 3D bicontinuous ordered ceramic and polymer microchannels for all-solid-state batteries. Energy Environ Sci 11:185–201

Zeng W, Shu L, Li Q, et al (2014) Fiber-based wearable electronics: A review of materials, fabrication, devices, and applications. Advanced Materials 26(31):5310–5336

Zheng H, Li J, Song X, et al (2012) A comprehensive understanding of electrode thickness effects on the electrochemical performances of Li-ion battery cathodes. Electrochimica Acta 71:258–265